

**Weak Shear Study of Galaxy Clusters by Simulated Gravitational  
Lensing**

by  
David Coss

A DISSERTATION

Presented to the Faculty of the Graduate Schools of the

UNIVERSITY OF MISSOURI – ST. LOUIS

AND

MISSOURI UNIVERSITY OF SCIENCE AND TECHNOLOGY

In Partial Fulfillment of the Requirements for the Degree

DOCTOR OF PHILOSOPHY

In

PHYSICS

2010

Approved by

Ricardo Flores, Chair

Bruce Wilking

John Schmitt

Jerry Peacher

Ron Cytron

©2010

David Coss

All Rights Reserved

## Abstract

Gravitational lensing has been simulated for numerical galaxy clusters in order to characterize the effects of substructure and shape variations of dark matter halos on the weak lensing properties of clusters. In order to analyze realistic galaxy clusters, 6 high-resolution Adaptive Refinement Tree N-body simulations of clusters with hydrodynamics are used, in addition to a simulation of one group undergoing a merger. For each cluster, the three-dimensional particle distribution is projected perpendicular to three orthogonal lines of sight, providing 21 projected mass density maps. The clusters have representative concentration and mass values for clusters in the concordance cosmology. Two gravitational lensing simulation methods are presented. In the first method, direct integration is used to calculate deflection angles. To overcome computational constraints inherent in this method, a distributed computing project was created for parallel computation. In addition to its use in gravitational lensing simulation, a description of the setup and function of this distributed computing project is presented as an alternative to in-house computing clusters, which has the added benefit of public enrollment in science and low cost. In the second method, shear maps are created using a fast Fourier transform method. From these shear maps, the effects of substructure and shape variation are related to observational gravitational lensing studies. Average shear in regions less than and greater than half of the virial radius demonstrates distinct dispersion, varying by 24% from the mean among the 21 maps. We estimate the numerical error in shear calculations to be of the order of 5%. Therefore, this shear dispersion is a reliable consequence of shape dispersion, correlating most strongly with the ratio of smallest-to-largest principal axis lengths of a cluster isodensity shell. On the other hand, image ellipticities, which are of great importance in mass reconstruction, are shown to have very little variance. However, tangential alignment of average image distortion is quite strong, making mass den-

sity peak locations easily resolvable, in contrast to average convergence and overall ellipticity of isodensity regions.

## Acknowledgments

I would like to acknowledge and thank the NASA-Missouri Space Grant Consortium for its financial support of my work, providing me with the time and freedom to concentrate on my research. Of course, that work would not have happened without a place to encourage and foster scientific thought. For that I have the Physics department of the University of Missouri – St Louis to thank. I would like to thank Bruce Wilking, Ron Cytron, John Schmitt and Jerry Peacher for taking time out of their busy schedules to serve on my dissertation committee. For all of his invaluable suggestions, discussions and writing critiques, I would like to thank Ricardo Flores. The research described in this text would not have taken place without the support of the volunteer computing community. For allowing me to use their computers, I would like to show my appreciation for the entire BOINC community, including alpha and beta testers, dedicated volunteers, unpaid support people, and people within my project who enthusiastically followed a small one-person project. Also, I would like to thank the developers at UC Berkeley for keeping BOINC open source, so that people like myself can use it freely. For his multiple  $\text{\LaTeX}$  tips and suggestions, as well as his general camaraderie, I thank Dan Blake. For imparting upon me knowledge of many things general relativistic and serving as a model teacher, I want to show my appreciation for Ta-Pei Cheng. Of course, all of this was possible only with the continuous support of my family, both immediate and extended, getting me to this point and beyond. Last but definitely not least, I would like to thank my wife, Diana, for her constant patience and support for me during this process.

# Contents

<b>Acknowledgments</b>	<b>v</b>
<b>List of Tables</b>	<b>viii</b>
<b>List of Figures</b>	<b>x</b>
<b>1 Introduction</b>	<b>1</b>
1.1 Highlights in Development of Weak Lensing . . . . .	3
<b>2 Basics of Gravitational Lensing</b>	<b>10</b>
2.1 Gravitational Light Deflection . . . . .	10
2.2 Lensing as a Mapping . . . . .	13
2.3 Characteristics of Gravitational Lensing . . . . .	14
2.4 Specific Properties of Weak Lensing . . . . .	19
<b>3 Dark Matter</b>	<b>22</b>
3.1 Disagreement between Studies of Luminosity and Dynamics . . . . .	22
3.2 Dark Matter Theory . . . . .	24
3.3 Dark Matter Halo Shape . . . . .	25
3.3.1 Shape Studies . . . . .	25
3.3.2 Density Profiles . . . . .	26
3.4 Mass Reconstruction Methods . . . . .	29
<b>4 Deflection Angle Calculation and Ray Tracing</b>	<b>33</b>
4.1 Usefulness of Deflection Angle Calculations . . . . .	33
4.2 Procedure . . . . .	33
4.3 Volunteer Computing: BRaTS@Home . . . . .	36
4.4 Impact of Distributed Computing . . . . .	38
4.5 Verification of Accuracy . . . . .	40

<b>5</b>	<b>Numerical Calculation of Shear</b>	<b>43</b>
5.1	Calculation of Shear via Convolution of Convergence . . . . .	43
5.2	Shear Calculation . . . . .	44
5.3	Comparisons with Analytical Solutions . . . . .	46
<b>6</b>	<b>Correlation Study of Mass Ellipticity and Shear</b>	<b>50</b>
6.1	Galaxy Cluster Distributions . . . . .	50
6.2	Results for Calculated Shear . . . . .	53
<b>7</b>	<b>Discussion</b>	<b>61</b>
<b>8</b>	<b>Summary</b>	<b>69</b>
<b>A</b>	<b>Generation of Mass Distributions for Numerical Simulation</b>	<b>71</b>
<b>B</b>	<b>Calculation of Lensing Properties of the NFW Profile</b>	<b>73</b>
	<b>References</b>	<b>76</b>
	<b>Vita</b>	<b>80</b>

## List of Tables

4.1	BRaTS@Home and overall BOINC Statistics as of April 11, 2010 . . .	40
4.2	Numerical and Analytical Deflection Angle Comparison . . . . .	42
6.1	Simulated Cluster Data . . . . .	51
6.2	Orientations of Simulated Cluster. . . . .	52
6.3	Resolution data for cluster convergences. . . . .	52
6.4	Average shear values for simulated clusters. . . . .	54
6.5	Average image axial ratio values for simulated clusters. . . . .	55
6.6	Difference in shear between quadrants as a percentage of the spherical cluster value . . . . .	56

## List of Figures

1.1	Arcs produced by gravitational lensing. Images reproduced with permission of author (Lynds & Petrosian 1989).	7
2.1	Schematic illustration of Gravitational Light Deflection . . . . .	10
2.2	Ray-trace images of a background source lensed by a point mass. . . . .	15
2.3	Source and ray-trace images showing parity inversion. . . . .	16
2.4	Plot of image locations. . . . .	18
2.5	Images of a row of circular sources. . . . .	18
2.6	Illustration of effects of shear and convergence. . . . .	20
4.1	Ray Trace Class Diagram . . . . .	35
4.2	Organizational Diagram for the BOINC System BRaTS@Home . . . . .	37
4.3	Deflection angle for a $3 * 10^{11} M_{\odot}$ circular lens. . . . .	41
5.1	Simulated triaxial NFW distribution with lens (source) redshift of $z = 0.3$ ( $0.7$ ). $M_{vir} = 2 * 10^{14} h^{-1} M_{\odot}$ , $R_{vir} = 1200 h^{-1} kpc$ , $c = 4.8$ , $q = 0.8$ , $s = 0.5$ and semi-major axis is placed along $\theta = \phi = \frac{\pi}{4}$ using a log scale.	45
5.2	Isothermal sphere located at $z = 0.35$ , with background sources at $z = 0.8$ , with an Einstein radius of $0.97 h^{-1} kpc$ . . . . .	47
5.3	Percent error for triaxial nfw convergence and FFT-calculated shear, compared to values found through numerical integration. Radial distance extends to the virial radius. . . . .	49
6.1	Shear map of cluster 5 projected perpendicular to the X-axis. Axes are labeled in units of the virial radius. . . . .	57
6.2	Convergence of cluster 5 projected perpendicular to the X-axis. Axes are labeled in units of the virial radius. . . . .	58
6.3	Shear map of cluster 5 projected along the Z-axis. Axes are labeled in units of the virial radius. . . . .	59

6.4	Convergence of cluster 5 projected perpendicular to the Z-axis. Axes are labeled in units of the virial radius. . . . .	60
7.1	Plot of corresponding shear and mass values. Masses are given in units of $10^{14} h^{-1} M_{\odot}$ . . . . .	62
7.2	Plot of corresponding shear and concentration values. . . . .	63
7.3	Plot of corresponding shear and axial ratio $q$ values. . . . .	64
7.4	Plot of corresponding shear and axial ratio $s$ values. . . . .	65
7.5	Plot of corresponding convergence and axial ratio $s$ values. . . . .	65
7.6	Plot of corresponding convergence and total mass values. Mass is given in units of $10^{14} h^{-1} M_{\odot}$ . . . . .	66
7.7	Plot of corresponding convergence and concentration parameter values. . . . .	67
7.8	Plot of corresponding convergence and shear parameter values, for distances greater than $0.5R_{vir}$ . . . . .	68

# 1 Introduction

Beginning with the discovery of a discrepancy between stellar and galactic mass-to-light ratios, the study of a form of matter which interacts only noticeably through the gravitational force has become an active field of study in Physics, both in astrophysical and laboratory settings. While laboratory experiments continue to search for a particle basis for dark matter, galaxies and galaxy clusters serve as a stage for the study of dark matter halo properties, such as shape, mass composition (i.e. dark versus luminous) and self-interaction strength. Such astrophysical studies take place in gravitational lensing observation. While gravitational lensing has provided the means to reconstruct projected dark matter mass density, numerical N-body simulations have probed the properties of dark matter halos, up to computational resolution limitations. From such numerical simulations it has become clear that galaxy clusters, which are dominated by dark matter, should exhibit a broad distribution of ellipticity, for a given total mass. As wider and deeper imaging surveys become available, it will be necessary to understand what effect this noted dispersion has on observations. These effects are quantified and discussed below for the case of weak gravitational lensing.

Within cosmology literature, there exists a variety of notations and usages of parameters. For clarity, the following is a summary of the notation used throughout this text. All of the material and calculations here are presented in the context of the concordance model. Mass and distance quantities are written using the Hubble parameter,  $h$ , such that Hubble's constant is  $H_0 = h * 100km/s/Mpc$ . Unless otherwise noted, when cosmological parameters, such as dark matter density,  $\Omega_m$ , are needed for calculations, these parameters are taken from the five-year Wilkinson Microwave Anisotropy Probe (WMAP) data set (Hinshaw et al. 2009). While seven-year WMAP data has been recently released (Jarosik et al. 2010), the largest effect of changes to the data set is found in the  $\sigma_8$  parameter, which measures the

RMS amplitude of mass fluctuations within spheres of radius  $8h^{-1} Mpc$ . However, the changes in  $\sigma_8$  have a negligible effect on the axial ratios of the clusters used here (Allgood et al. 2006). Distances represented with a capitalized “D” denote angular diameter distances, which is the pertinent distance in gravitational lensing studies. Also, to remove ambiguity between positions in either source or lensing planes and Cartesian coordinates, throughout this text symbols “x” and “y” will represent positions in the lensing and source planes, respectively, while subscripts will represent orthogonal Cartesian coordinates, e.g.  $x_1$  and  $x_2$ . Finally, all equations presented in this work were obtained from the cited sources. Gravitational lensing equations of the general nature may be found derived in Schneider et al. 1999.

This work is organized as follows: the remainder of this section highlights the development of gravitational lensing to the study of weak lensing. Studies which illustrate an important method of lensing analysis are included here. For a more detailed history, and for information on strong and microlensing, which is not used in this work, see Schneider et al. 1999 and Schneider et al. 2006. Section 2 provides the theoretical foundation for gravitational lensing studies, specifically focusing on those principles which are important in this work. Next, the theory of dark matter is outlined in two ways. Sections 3.1 and 3.2 present historical background for the theory of dark matter. Following this is a discussion of dark matter halo shape, in Section 3.3, which is a motivating factor of this work. Section 3.4 provides a summary of two observational methods used to reconstruct mass densities. After providing the principles and motivation for this study, the methods are outlined, beginning with deflection angle by ray-tracing in Section 4 and ending with shear calculations in Section 5. Included in Section 4 is an outline of a distributed computing project, including its operational procedure and impact on the science involved and volunteers participating in the project. Finally, the results are presented in Section 6, followed by a discussion.

## 1.1 Highlights in Development of Weak Lensing

From the eighteenth century studies of Michell and Laplace<sup>1</sup> to modern mass reconstruction methods, gravitational lensing has evolved from an esoteric study of gravitational effects on light to a tool used to probe properties of astrophysical structures and phenomena. An early example of the calculation of light deflection by gravity was developed by Johann Georg von Soldner in 1804, when Soldner used the classical mechanics approach to study the path of light rays passing a massive object (Soldner 1804). Soldner calculated the amount of error one could expect due to gravitational deflection when measuring locations of stellar objects. To perform this calculation, however, Soldner assumed light had “all of the absolute properties of matter” (ibid, page 171). Using this assumption, within the framework of classical mechanics, Soldner’s result produces a deflection angle of

$$\hat{\alpha}(r) = \frac{2GM}{c^2 r}, \quad (1.1)$$

where  $G$  is the gravitational constant of Newtonian mechanics,  $M$  is the mass of the deflecting object and  $c$  is the vacuum speed of light.

Roughly 100 years after Soldner’s light deflection calculation, Albert Einstein studied the propagation of light within the framework of special relativity (Einstein 1911). As one part of this study, Einstein shows the speed of light will appear to vary with position due to the gravitational potential through the use of the equivalence principle. Applying Huygen’s Principle to a light wave traveling through a gravitational potential, Einstein derived a deflection angle equal to Soldner’s value, though Einstein made no mention of Soldner’s work. At the end of this 1911 paper, the deflection angle for a light ray passing near the Sun is calculated to be 0.83 arc-seconds.

---

<sup>1</sup>Independently, John Michell and Peter Simon Laplace noted that if the mass of an object was sufficiently large, the escape velocity could exceed the speed of light, by assuming light is affected by gravity like material objects (cf Schneider et al. 1999).

Five years later, Einstein revised the light deflection angle relationship, using it as one of a few predictions of the general theory of relativity (Einstein 1916). In the special relativistic case, the bending of the light ray is due to the observed speed of light change by a factor of

$$1 + \frac{\Phi}{c^2}, \quad (1.2)$$

where  $\Phi$  is the gravitational potential. This effect is a result of gravitational time dilation, as the time interval is being enhanced by this amount. However, within general relativity the effects of gravity both on space and time are taken into account. In relativity, displacements are found in any particular frame of reference by,

$$ds^2 = g_{\mu\nu} dx^\mu dx^\nu, \quad (1.3)$$

where  $ds$  represents the invariant displacement interval and  $dx^\mu$  represents the infinitesimal displacement in the  $\mu$ -direction in the frame of reference in which the values of the metric,  $g_{\mu\nu}$ , are calculated. As a simple example, applicable to the Sun, consider a weak, static gravitational potential,  $\Phi(r)$ , in spherical space-time coordinates  $(t, r, \phi, \theta)$ . In this coordinate system, the non-trivial values of  $g_{\mu\nu}$  are

$$g_{tt} = - \left( 1 + \frac{2\Phi}{c^2} \right) \quad (1.4)$$

$$g_{rr} = \left( 1 + \frac{2\Phi}{c^2} \right)^{-1} \quad (1.5)$$

$$g_{\theta\theta} = g_{\phi\phi} = 1. \quad (1.6)$$

Using the displacement equation, the observed speed of light equals

$$c(r) = c \sqrt{-\frac{g_{tt}}{g_{rr}}} \quad (1.7)$$

$$= c \left( 1 + \frac{2\Phi}{c^2} \right). \quad (1.8)$$

Applying the Huygen's principle and integrating along the path with this general relativistic value gives a deflection angle twice the previously calculated one, equal to

$$\hat{\alpha}(r) = \frac{4GM}{c^2 r}. \quad (1.9)$$

Using this result, Einstein calculated the deflection angle of a light ray passing the surface of the Sun to be 1.7 arc-seconds (Einstein 1916). Three years later, this result was tested by Arthur Eddington through the observation of star positions near the Sun, viewed during the May 29, 1919 solar eclipse (Dyson et al. 1920). Star positions were measured at two sites, the Island of Principe, off of the western coast of Africa, and Sobral in North Brazil. The deflection angle values measured were  $1.98 \pm 0.12$  arc-seconds (Sobral) and  $1.61 \pm 0.30$  arc-seconds (Principe)<sup>2</sup>. About these deflection angles, Dyson et al. 1920 wrote,

*Thus the results of the expeditions to Sobral and Principe can leave little doubt that a deflection of light takes place in the neighborhood of the sun and that it is of the amount demanded by Einstein's generalized theory of relativity, as attributable to the sun's gravitational field.*

Alongside Einstein's predicted light deflection by the Sun, Fritz Zwicky suggests using galaxies as sources of gravitational lensing (Zwicky 1937a). Zwicky lists three reasons to search for gravitational lensing images in galaxies. First, lensing could serve as an additional test of general relativity. Second, though Zwicky does not use the term lens, he does suggest using the phenomenon as method of seeing objects beyond the scope of conventional telescopes. Finally, it could be used as an alternative method of measuring galaxy masses.

In 1964, Sjur Refsdal illustrated the possibility of using gravitational lensing as a

---

<sup>2</sup>The error reported with these deflection angles is less than the seeing. This was achieved by averaging multiple images.

tool for cosmology (Refsdal 1964). Refsdal suggested using the time delay between multiple images of the same supernova source. Assuming the deflecting galaxy is spherically symmetric and both the supernova and deflecting galaxy are at low redshifts, Refsdal shows that the inferred mass of the galaxy scales linearly with the time delay, while the time delay and Hubble’s constant share an inverse relationship. After establishing these relationships, Refsdal goes on to show the observation of this image time delay is possible using average galaxy densities and masses known at the time. Essentially, this paper encourages the beginning of a field of study known as microlensing. For more information on microlensing, see Schneider et al. 2006.

One of the next major discoveries in gravitational lensing is the observation of arcs. In 1986, Roger Lynds and Vahé Petrosian reported the observation of “arclike features” in images of the clusters Abell 370 and CL 2244-02, which themselves are at redshifts of 0.373 and 0.328, respectively (Lynds & Petrosian 1986), as shown in Figure 1.1. These observations came after it was noted that similar but less “clearly delineated” features were found in the cluster Abell 2218 (Lynds & Petrosian 1989, page 1).

The lengths and radii of curvature of the arcs in the images of both clusters are similar and have the feature of being concave inward towards the center of the structure of the clusters. Additionally, spectroscopic analysis places the Abell 370 arc at a redshift of 0.725 (Miller & Goodrich 1988). While this separate redshift would now be one factor in naming this a gravitational lensing image, in 1989, Lynds & Petrosian acknowledge (ibid, page 6),

*We are continually reminded by colleagues that not all astronomers place unrestrained faith in the cosmological interpretation of redshift for extragalactic objects.*

Therefore, Lynds & Petrosian 1989 rule out explanations ranging from tidal disruptions of a galaxy to shock waves before finally settling on the gravitational lensing

explanation.

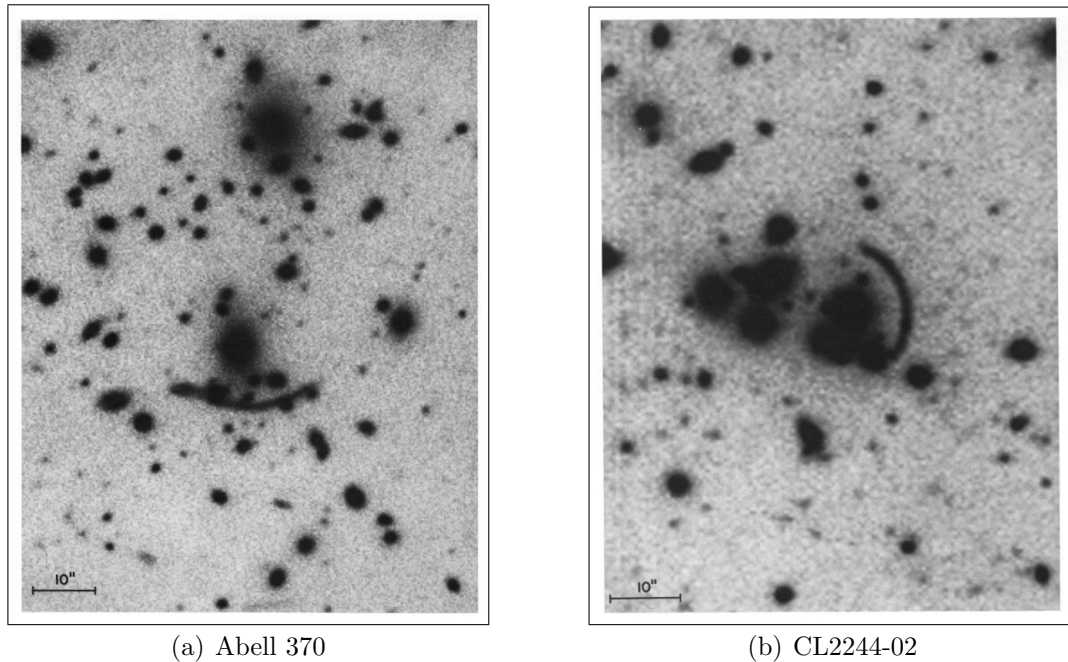


Figure 1.1: Arcs produced by gravitational lensing. Images reproduced with permission of author (Lynds & Petrosian 1989).

With the improvement of computing power and the advent of CCD astronomy, gravitational lensing observations moved into the weak lensing regime. One groundbreaking work in the area of weak lensing is Tyson et al. 1990. A statistical analysis of the image alignments of galaxies in Abell 1689 and CL 1409+52 selected by color type revealed tangential alignment around the center of both clusters. This tangential alignment is most distinct among blue galaxies, which are located at a higher redshift. While Abell 1689 and CL 1409+52 are at redshifts of 0.18 and 0.46, respectively, seventy percent of the faint blue galaxies are at a redshift exceeding 0.9. Additionally, Tyson et al. 1990 perform ray-tracing simulations with isothermal mass distributions, using real deep field images as background sources. The same tangential alignment study was then performed on these ray-trace results, showing a direct relationship between velocity dispersion and tangential alignment strength.

Once the tangential alignment and image distortion effects are shown to be the

result of gravitational lensing, the next step would be to use lensing as a tool to study astrophysical structures. As mentioned above, it had been demonstrated that gravitational lensing can constrain galaxy mass and Hubble’s constant (Refsdal 1964). Another useful application of gravitational lensing was to constrain mass density profiles within the center of lensing clusters (Hammer 1991). However, Kaiser & Squires 1993 utilize the weak lensing observations to reconstruct two-dimensional dark matter distributions. Image ellipticities are used to create a two-dimensional map of the shear and tangential alignment effects of gravitational lensing. Through the use of the differential equations that relate shear and two-dimensional mass density, Kaiser & Squires 1993 produce a projected matter distribution of the lensing mass distribution. The reconstruction method is tested with simulated isothermal models, one of which is chosen to represent the Abell 1689 studied by Tyson et al. 1990. Reconstruction reproduced the model density profile very well up to a constant offset. This mass offset is chosen so that the two-dimensional mass density reaches zero at the edge of the grid. A more detailed description of weak lensing mass reconstruction is provided in Section 3.4.

Weak gravitational lensing studies require wide surveys containing multiple galaxies to provide a sample set large enough for adequate image ellipticity averaging. Since weak lensing is based on the overall statistical analysis of galaxy images, it is vitally important to have a sufficiently high signal-to-noise ratio. One planned survey is the Large Synoptic Survey Telescope (LSST; cf LSST 2010). This telescope will have a  $9.6 \text{ deg}^2$  field of view. It is estimated that the shear noise with this survey will be  $0.05 \text{ arcmin}^{-2}$  (ibid, page 502). As is demonstrated below, this low noise level<sup>3</sup> will require an understanding of the effects of halo ellipticity dispersion on the average shear. Techniques which will be used to analyze LSST data directly use the average shear, or reduced shear, within an annulus around the center of the cluster. One

---

<sup>3</sup>compare to shear dispersion shown in Section 6.2.

example is surface density (ibid, Equation 14.10),

$$\Delta\Sigma(R) = \gamma_T(R)\Sigma_{CR}, \quad (1.10)$$

where  $\Sigma(R)$ , the projected mass density at a radial distance,  $R$ , is related to the tangential shear,  $\gamma_T$ . In this equation,  $\Sigma_{CR}$  represents the critical lensing density, which distinguishes different lensing regimes (cf Sections 2.3 & 2.4). Another example is the convergence (ibid, Equation 14.14)

$$\kappa(R) = 1 - \frac{1}{1 - g(R)} \exp\left(-\int_R^{R_M} \frac{2\langle g \rangle}{r(1 - \langle g \rangle)} - \frac{2\langle g(R_M) \rangle}{\alpha}\right) \quad (1.11)$$

through which the mass density, which is proportional to  $\kappa$  (cf Section 2.1), is related to the reduced shear,  $g$ , averaged within an annulus  $R < r < R_M$ . The average shear value within a given region plays an important role in galaxy cluster weak lensing studies. However, the average shear values do not simply depend on the lensing mass, instead depending on a combination of the magnitude and spacial distribution of the mass. One demonstrated feature of the CDM cosmology is the dispersion in shape parameters for dark matter halos of a given mass (cf Allgood et al. 2006 (simulation) and Mandelbaum et al. 2006 (observation)). For example, there exists a wide dispersion in ellipticity values. Below it is shown that this spread in halo ellipticity results in an equally broad range of average shear values, as are used in observation methods described above. Additionally, as surveys become broader and deeper, such as the LSST, this shear dispersion is on the order of the signal-to-noise ratio, therefore becoming observable.

## 2 Basics of Gravitational Lensing

### 2.1 Gravitational Light Deflection

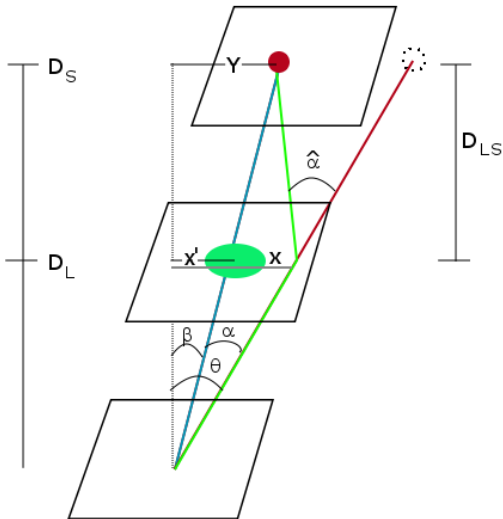


Figure 2.1: Schematic illustration of Gravitational Light Deflection

One of the successful predictions of Albert Einstein's theory of general relativity is the deflection of light ray paths due to the effects of gravitation (Einstein 1916). Similar to trajectories of massive objects, light rays experience a deflection effect. General Relativity gives the deflection angle,  $\hat{\alpha}$ , for a light ray passing a point mass,  $M$ , with impact parameter  $\vec{x}$  as

$$\vec{\hat{\alpha}}(\vec{x}) = \frac{4GM}{c^2} \frac{\vec{x} - \vec{x}'}{|\vec{x} - \vec{x}'|^2}, \quad (2.1)$$

where  $\vec{x}'$  is the location of the point mass,  $G$  is the Gravitational Constant of Newtonian Mechanics, and  $c$  is the speed of light. One may notice that this is simply

$$\vec{\hat{\alpha}} = 2R_{\star} \frac{\vec{x} - \vec{x}'}{|\vec{x} - \vec{x}'|^2}, \quad (2.2)$$

where  $R_{\star}$  is the Schwarzschild radius<sup>4</sup>. Since masses are often given in solar masses, it may be convenient to note that the Schwarzschild radius of the Sun is approximately 2.95km.

In the thin lens approximation, valid for cosmological distances because deflection occurs over distance scales much less than the line-of-sight distances, the lens may be treated as a two-dimensional deflector. Such projected planes of background objects and foreground lenses are illustrated in Figure 2.1. The thin lens approximation allows one to extend the deflection treatment given by Equation (2.1) to an extended body. If the mass is integrated over the projected mass density,  $\Sigma$ , then the deflection angle becomes

$$\vec{\alpha} = \frac{4G}{c^2} \int \Sigma(\vec{x}') \frac{\vec{x} - \vec{x}'}{|\vec{x} - \vec{x}'|^2} d^2x'. \quad (2.3)$$

As is sometimes done in other fields, such as electrodynamics, the unprimed factor in Equation (2.3) can be written as a gradient of a scalar potential, where the gradient is taken with respect to the unprimed variables. In other words, one may define  $\vec{\alpha} = \nabla \hat{\psi}$ , such that

$$\hat{\psi} = \frac{4G}{c^2} \int \Sigma(\vec{x}') \ln |\vec{x} - \vec{x}'| d^2x'. \quad (2.4)$$

In light of the two lensing regimes, strong and weak, it is convenient to write the surface mass density in terms of the critical density,

$$\Sigma_{cr} = \frac{c^2}{4\pi G} \frac{D_S}{D_{LS}D_L}, \quad (2.5)$$

where  $D_{LS}$  is the angular diameter distance between the lens and the source<sup>5</sup>. The physical interpretation and significance of  $\Sigma_{cr}$  is discussed further in Section 2.3.

<sup>4</sup>The symbol,  $R_{\star}$ , should not be confused with the Solar radius,  $R_{\odot}$ , which should also not be confused with the NFW scale radius,  $R_s$ . This notation will be used throughout.

<sup>5</sup>On cosmological scales,  $D_{LS}$  does not simply equal the difference  $D_S - D_L$ . Instead, relativistic effects must be considered. For a numerical relationship between redshift and distance, see Demianski et al. 2003.

Once this substitution has been made, one may obtain a useful quantity in lensing, the convergence.

Convergence is a measure of isotropic focusing of light rays. Using angular relationships shown in Figure 2.1, convergence can be related to the light deflection angle as follows. It can be seen in Figure 2.1 that

$$\vec{y} = \frac{D_S}{D_L} \vec{x} - D_{LS} \vec{\alpha}. \quad (2.6)$$

While Equation (2.3) is a function of linear distance in the lens plane, the deflection angle may be found as a function of light ray coordinate angles using the relationships,  $y = D_S \beta$  and  $x = D_L \theta$ , obtaining

$$\vec{\beta} = \vec{\theta} - \frac{D_{LS}}{D_S} \vec{\alpha}(D_L \theta). \quad (2.7)$$

At this point it is convenient to scale alpha to the point of view of the observer. The geometric meaning of the scaled and unscaled values of  $\alpha$  is shown in Figure 2.1. This gives the more familiar lens equation

$$\vec{\beta} = \vec{\theta} - \vec{\alpha}(\vec{\theta}), \quad (2.8)$$

where

$$\vec{\alpha}(\vec{\theta}) = \frac{1}{\pi} \int d^2 \theta' \kappa(\vec{\theta}') \frac{\vec{\theta} - \vec{\theta}'}{|\vec{\theta} - \vec{\theta}'|^2}, \quad (2.9)$$

using the definition of convergence

$$\kappa(\theta) = \frac{\Sigma(D_L \theta)}{\Sigma_{cr}}. \quad (2.10)$$

This definition of the deflection angle connects the aforementioned lensing potential,

$\psi$ , with convergence via the two-dimensional Poisson equation,

$$\nabla^2 \psi = 2\kappa. \quad (2.11)$$

This equation will be important in the study of shear.

## 2.2 Lensing as a Mapping

Viewing images and their sources in terms of positions in the lens and source planes can be represented as a mapping. Such a treatment of lensing leads to simple connections between mass density and image distortions, instead of point-by-point angle deflection. To treat lensing as a vector transformation, one first must find the Jacobian matrix, from which changes in positions between source and lensing planes may be found. Using the position variables defined above, the Jacobian matrix takes on the form,

$$A_{ij} \equiv \frac{\partial \beta_i}{\partial \theta_j}. \quad (2.12)$$

After finding the transformation matrix,  $A$ , at a given point, one immediately can understand the effects lensing has on extended background sources.

Viewing the Jacobian Matrix,  $A$ , in terms of the lensing treatment developed in Section 2.1, one can obtain the gravitational lensing quantities, convergence and shear. After substituting the lens equation into the definition of the Jacobian matrix,  $A$ , the Jacobian can be rewritten as,

$$A_{ij} = \delta_{ij} - \frac{\partial^2 \psi}{\partial x_i \partial x_j}. \quad (2.13)$$

From this, shear and convergence can be recovered:

$$tr A = 2 - \nabla^2 \psi = 2(1 - \kappa), \quad (2.14)$$

$$det A = \left(1 - \frac{\partial^2 \psi}{\partial x_1^2}\right) \left(1 - \frac{\partial^2 \psi}{\partial x_2^2}\right) - \left(\frac{\partial^2 \psi}{\partial x_1 \partial x_2}\right)^2, \quad (2.15)$$

$$\equiv (1 - \kappa)^2 - \gamma_1^2 - \gamma_2^2. \quad (2.16)$$

Shear has been defined here by

$$\gamma_1 = \frac{1}{2} \left( \frac{\partial^2 \psi}{\partial x_1^2} - \frac{\partial^2 \psi}{\partial x_2^2} \right), \quad (2.17)$$

$$\gamma_2 = \frac{\partial^2 \psi}{\partial x_1 \partial x_2}, \quad (2.18)$$

$$\gamma \equiv \gamma_1 + i\gamma_2. \quad (2.19)$$

In these two-dimensional calculations, as well as with Fourier analysis used in Section 5.1, it is advantageous to treat shear as a complex number, as in Equation (2.19).

Now  $A$  can be viewed as a symmetric, 2x2 matrix with eigenvalues of  $1 - \kappa \pm \gamma$ ,

$$A = \begin{bmatrix} 1 - \kappa - \gamma_1 & -\gamma_2 \\ -\gamma_2 & 1 - \kappa + \gamma_1 \end{bmatrix}. \quad (2.20)$$

## 2.3 Characteristics of Gravitational Lensing

Defining magnification in terms of the determinant of the Jacobian,

$$\mu = \frac{1}{det A}, \quad (2.21)$$

makes interesting properties of light deflection more apparent. Immediately, one notices that should the determinant of the Jacobian go to zero, magnification becomes infinite. This is an artifact, however, that is due to the ray treatment of optics here. Points in the lensing plane for which the determinant vanishes form what are known

as critical curves. Tracing the critical curves back to the source plane lead to caustics. In the case of axial symmetry, critical curves are circles. In the limit that the circular lens becomes a point mass, the caustic becomes a point. A background source located at that point forms a so-called Einstein ring, as shown in Figure 2.2(a).

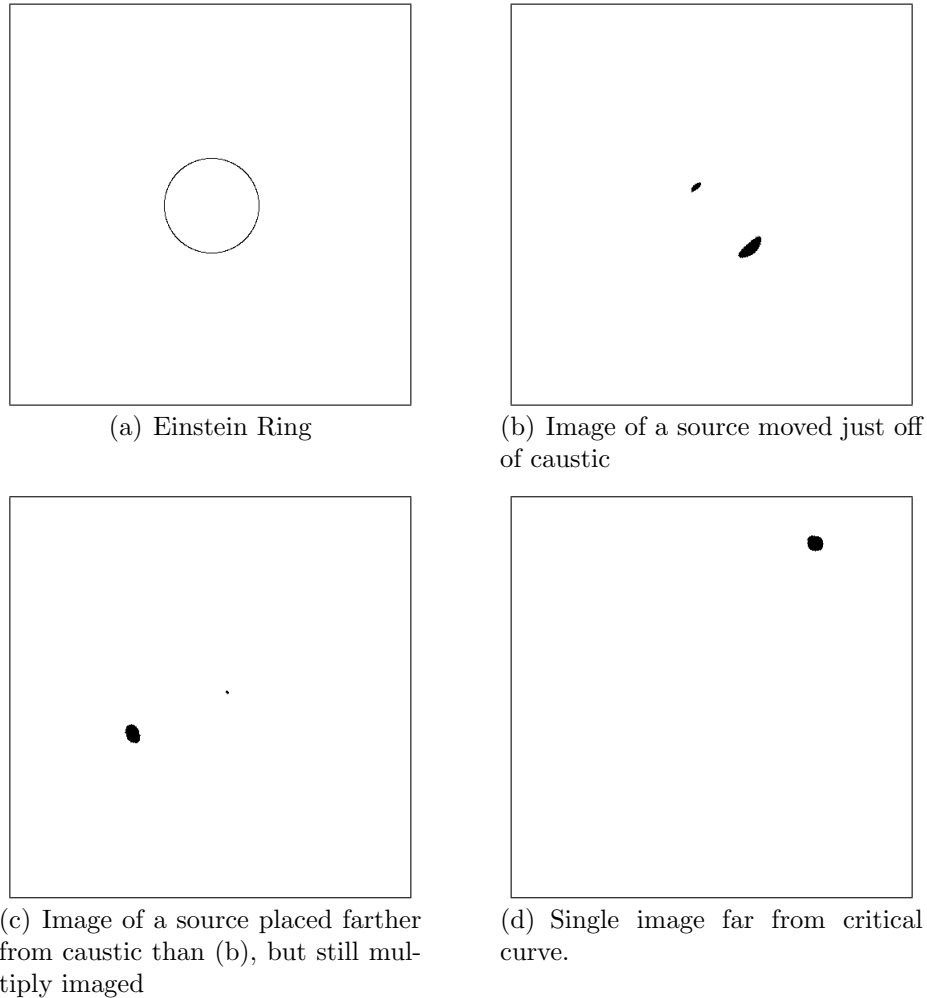


Figure 2.2: Ray-trace images of a background source lensed by a point mass.

Since magnification diverges for points lying on critical curves, unphysical infinite magnification must be reconciled with diverging mathematical formulae. Extended sources do not have simple magnifications corresponding to values at a point. Instead, a mean value of the extended source contributes to the real magnification factor. Further, Schneider et al. 1999 show finite magnification even for point sources, using

wave properties, which have been suppressed in this geometric analysis.

Critical curves separate regions of varying sign of the determinate of the Jacobian matrix. The sign of the determinant designates the parity, or orientation, of the images. Figure 2.3 shows the effect of parity change on different sides of a critical curve, using the same lens as in Figure 2.2. Here an arrow was placed in the source plane near the caustic along with a point located at the caustic, to provide the Einstein ring for illustrative purposes. Ray-tracing demonstrates parity inversion, as well as the image position with respect to the critical curve. Outside of the critical curve, the image is upright, having positive parity. Within the critical curve, the image has negative parity.

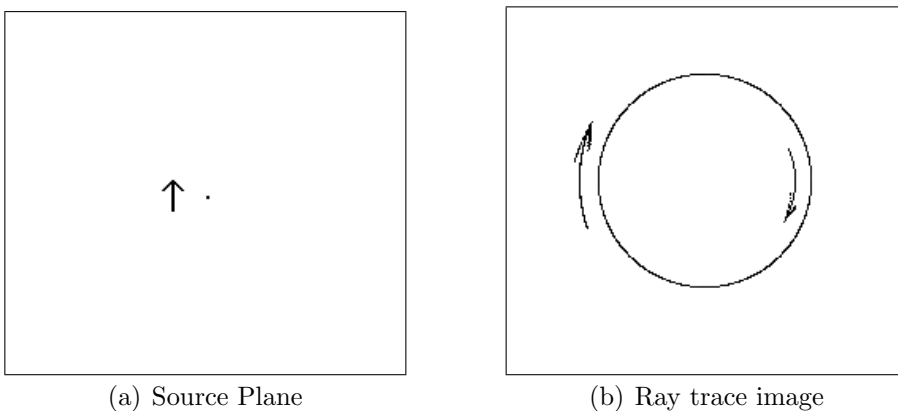


Figure 2.3: Source and ray-trace images showing parity inversion.

Under certain conditions, gravitational lenses can produce multiple images. A necessary condition is that there exists one or more points where the determinant is negative. In this case, each point has an image of negative parity, corresponding to the negative eigenvalue of the Jacobian. Schneider et al. 1999 show that there must exist at least two points of positive parity. Additionally, if there exists a point  $x_{MI}$  such that

$$\kappa(x_{MI}) > 1, \quad (2.22)$$

there can be multiple images. This condition, though sufficient, is not necessary. The

so called critical density,  $\Sigma_{cr}$ , gets its name from this condition. Mass distributions with  $\Sigma > \Sigma_{cr}$  are critical, or can produce multiple images.

The occurrence of multiple images and the critical density condition are best realized with a plot of positions and the deflection angle. Figure 2.4 shows the locations of images for a circular lens of constant mass density for three specific cases. The solid curve in this plot represents the deflection angle for a circular lens, with the center of the lens corresponding to the center of the plot. Dashed lines represents lines of  $\theta - \beta$ . According to the lens equation, the intersection of dashed and solid lines represent points where an image is produced at a distance from the center corresponding to the horizontal distance of the intersection in the plot. The three cases illustrated in Figure 2.4 show varying types of images. The top dashed line represents the case where one image is produced. The middle dashed line shows two images, where the image to the right of the origin lies on the critical curve. The bottom dashed line passes through the caustic point at the origin of the source plane. The outer two points on this curve represent the Einstein ring produced by this lens. Additionally, the spherical symmetry of this lens makes the critical nature of the critical density apparent. Should the slope of the inner region of  $\alpha$  become less than that of the  $\theta - \beta$  lines, multiple images cannot be produced.

The role of the critical density in the production of multiple images can be seen when developing a relationship for the average density. For a source directly behind a spherically symmetric mass density, the lens equation gives

$$\begin{aligned} \alpha &= \theta_E \\ &= \frac{M(< \theta_E)}{\pi \Sigma_{cr} D_L^2 \theta_E}. \end{aligned} \tag{2.23}$$

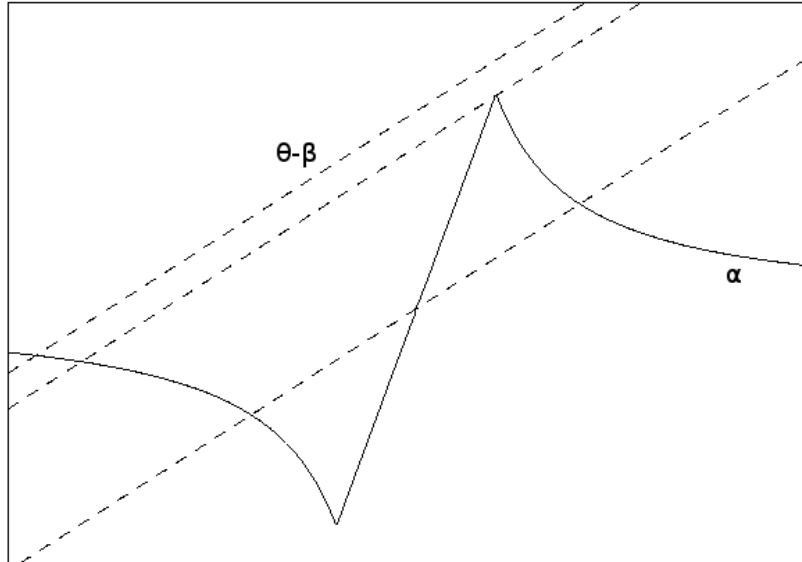


Figure 2.4: Plot of image locations.

Therefore the average mass density of the lens within  $\theta_E$ ,

$$\langle \Sigma(\theta_E) \rangle = \frac{M(< \theta_E)}{\pi D_L^2 \theta_E^2} = \Sigma_{cr}. \quad (2.24)$$

Therefore, if an Einstein ring can be produced by a lens, satisfying the condition in Equation (2.23), the average surface mass density within the ring is equal to the critical density. Clearly, if the density is less than the critical density everywhere, an Einstein ring cannot be produced. While this was developed for the spherically symmetric mass, this provides a good indication of the possibility of strong lensing and reflects the sufficient multiple lensing condition of Equation (2.22).



Figure 2.5: Images of a row of circular sources.

Figure 2.5 demonstrates both strong and weak lensing image types. This image was produced by placing a point mass in the center of the lensing frame and circular sources of equal radius along one horizontal line in the source plane lying above the lens. Next the image positions were found by ray-tracing the light ray backwards to the source plane. The black ring in the center of the diagram is the Einstein ring for this Schwarzschild, or point-mass, lens. Near the Einstein ring, one can see multiple imaging of the three sources closest to the center. Images on the right side within the Einstein ring correspond to sources to the left of the caustic point, in a manner illustrated by Figure 2.3(b), where only one non-caustic source was used. The left-most source is well outside of the lensing region, while the source next to it displays only weak lensing. Lensed images are aligned tangentially with the Einstein ring, which is centered around the lens, showing the Einstein ring is a tangential critical curve.

## 2.4 Specific Properties of Weak Lensing

Multiple images are the defining characteristic of strong lensing. In contrast, regions of small amounts of shear and convergence, i.e.  $\kappa \ll 1$  and  $\gamma \ll 1$ , will not produce multiple images. Such lensing is known as weak lensing.

In the weak lensing regime, circular background images are lensed to an ellipse, whose semi-major and semi-minor axes are oriented along the eigenvectors of  $A$ . However, characteristic of weak lensing, the change in the image ellipticity is minute. To illustrate this effect consider a circular source of radius,  $R$ . As demonstrated by the inverse of the Jacobian,  $A$ , the source is transformed to an ellipse with semi-major and semi-minor axes of length,

$$\Lambda_{\pm} \equiv \frac{R}{1 - \kappa \mp \gamma}, \quad (2.25)$$

respectively. From this image distortion, the anisotropic nature of shear becomes apparent. In the absence of shear<sup>6</sup> ( $\gamma \rightarrow 0$ ), the image remains circular, while becoming enlarged by a factor of  $\frac{1}{1 - \kappa}$  in all directions. In this sense, convergence causes isotropic magnification. However, in the presence of shear, there is preferential stretching along one of the eigenvectors of the transformation matrix. These distortions are illustrated in Figure 2.6.

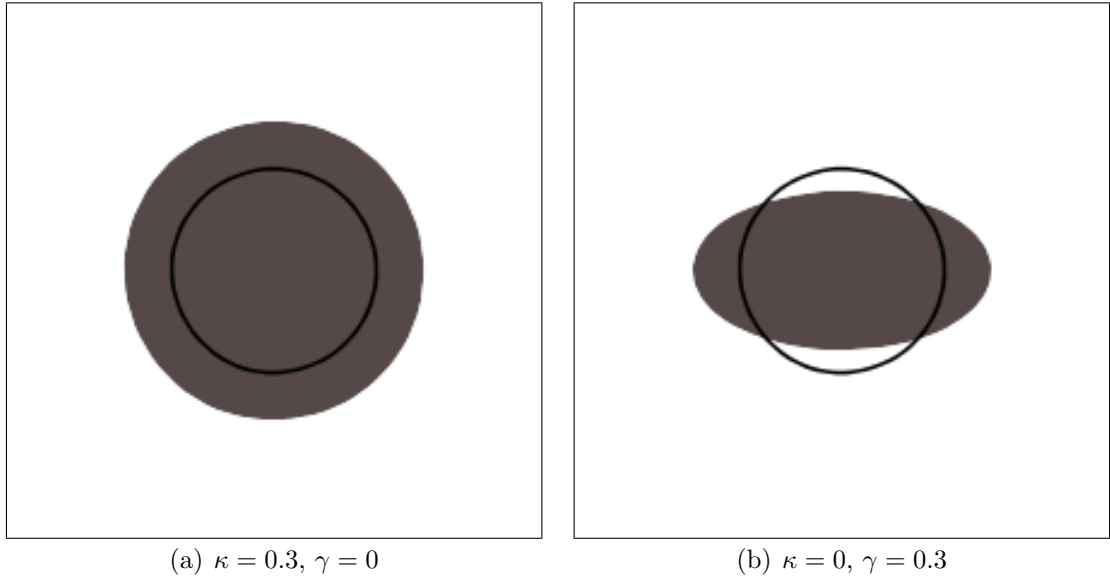


Figure 2.6: Illustration of effects of shear and convergence.

The second characteristic property of weak lensing is the systematic alignment of image ellipticity tangent to a circle centered around mass peaks. To illustrate this property, it is most useful to transform the shear from the Cartesian coordinate system, as defined by Equations (2.17) - (2.19), to tangential and cross components. In regards to this definition, namely the sign, there are some differences in the literature. Here, the convention of Schneider et al. 2006 will be used. An alternative definition

---

<sup>6</sup>This effect is artificially produced in Figure 2.6(b).

is used by Kaiser 1995. Following Schneider et al. 2006,

$$\gamma_t \equiv -\operatorname{Re} \{ \gamma e^{-2i\phi} \} \quad (2.26)$$

$$\gamma_\times \equiv -\operatorname{Im} \{ \gamma e^{-2i\phi} \} , \quad (2.27)$$

where  $\gamma_t$  and  $\gamma_\times$  are the tangential and cross components, respectively, and  $\phi$  is the azimuthal angle.

From the exponential function in these definitions, the polar nature of shear is apparent. Technically speaking, shear is not a vector. While a vector is transformed to itself under a  $360^\circ$  rotation, shear requires only  $180^\circ$ . For a circularly symmetric mass distribution,  $\vec{\alpha} = \hat{\alpha}(r)\hat{r}$ . In this case,  $\gamma_t = \gamma$  and  $\gamma_\times = 0$ . In regions of weak lensing, averaging shear in a small neighborhood reveals an overall tangential alignment around peaks in the mass density, as demonstrated in Figure 2.5.

The use of weak lensing as an observational tool is a relatively new technique, dating back to the pioneering work of Tyson et al. 1990. The need to average over large amounts of images to notice the overall image alignments characteristic of weak lensing makes this a particularly difficult task. The small shear involved in weak lensing generally implies minute changes in image ellipticity. Additionally, the original source ellipticities are not known. However, without a cause for source ellipse alignment, it is assumed that unlensed images would have random ellipse alignment after corrections for anisotropic point spread function (PSF). In other words, a nontrivial average ellipticity must be due to lensing, when no other source of alignment exists. Observing such a result requires a large sample of galaxies, in addition to imaging devices and techniques capable of resolving and averaging small images.

### 3 Dark Matter

#### 3.1 Disagreement between Studies of Luminosity and Dynamics

With gravitationally bound systems, the virial theorem may be applied as a means of obtaining the mass of the system. As a simple example, consider a spherical cloud of uniform density,  $\rho$ , such that the mass within a given distance,  $r$ , from the center is  $M(r) = \frac{4}{3}\pi r^3 \rho$ . The gravitational energy of particle of mass,  $m$ , within a distance,  $r$ , from the center of a spherical mass,  $M(r)$ , is given by

$$U(r) = -\frac{GM(r)m}{r}. \quad (3.1)$$

Drawing from the analogous result from electrostatics, the total binding energy can be shown to equal

$$U = -\frac{3}{5} \frac{GM^2}{R}. \quad (3.2)$$

For the above mass density in equilibrium, the virial theorem gives

$$\frac{1}{2} \sum_i^N m_i v_i^2 = \frac{1}{2} \frac{3}{5} \frac{GM^2}{R}. \quad (3.3)$$

If each of the  $N$  particles have equal mass,

$$\sum_i^N m_i v_i^2 = \frac{M}{N} \sum_i^N v_i^2 = M \langle v^2 \rangle. \quad (3.4)$$

Then

$$M = \frac{5}{3} \frac{R \langle v^2 \rangle}{G}. \quad (3.5)$$

For an isotropic velocity dispersion, the average velocity is the same in all directions, or  $\langle v^2 \rangle = \langle v_r^2 \rangle + \langle v_\theta^2 \rangle + \langle v_\phi^2 \rangle = 3 \langle v_r^2 \rangle = 3\sigma_r^2$ . Such a treatment of velocities

is analogous to the kinematic approach to thermodynamics of molecules. At the same time, the radial component of the velocity is the component measured by astronomers for these extra-galactic objects and is therefore the most advantageous to use in relation to mass and radius. Substituting this into Equation (3.5) gives

$$M = \frac{5R\sigma_r^2}{G}. \quad (3.6)$$

In the 1930's, Fritz Zwicky applied the virial theorem to the Coma Cluster (Zwicky 1937b). Based on measurements of the velocity dispersion, Zwicky obtains a lower limit of an average galaxy mass in the cluster to be  $4.5 * 10^{10} M_{\odot}$ . At the same time, Zwicky provides an average luminosity of  $8.5 * 10^7 L_{\odot}$ . After comparing the average mass-to-luminosity ratio of a Coma Cluster galaxy to that of the Kapteyn stellar system, Zwicky states, "this discrepancy is so great that a further analysis of the problem is in order" (ibid, page 232). Later in this paper, Zwicky suggests using galaxies as gravitational lenses as a better way of obtaining the mass of galaxies.

In 1970, Vera Rubin and Kent Ford measured the rotation velocities of the Andromeda Galaxy (Rubin & Ford 1970). In their paper, Rubin & Ford 1970 produce plots of rotation velocities based on their measurements of radial velocities, as measured by redshifts at various distances from the center of the galaxy, within the assumption of circular motion. However, while this study prompted the discussion of galaxy rotation curves and mass-to-light ratios, it lacked the radial extent throughout the galaxy to clearly demonstrate the need for dark matter. Indeed, the topic of non-luminous matter is not mentioned by Rubin and Ford at this point.

Using optical measurements to produce a rotation curve provides a limited view of the galaxy as a whole. However, including velocities derived from 21-cm Hydrogen observations extends the rotation curve much farther than the extent of the optical

portion of the galaxy. One such example is the 16 galaxy study by Kent 1987. Within this sample of galaxies, rotation curves are shown to remain flat beyond the galactic bulge. Attempts are made to reproduce these rotation curves based on mass profiles. Two curve fitting methods are used. With the first method, which Kent refers to as the “maximum-disk solution”, no halo was used and mass-to-light ratios are fit to the rotation data. With the second method, bulge, disk and halo parameters are adjusted to the rotation data. In regards to the first method results, Kent states,

*In no case does the maximum-disk solution produce a good fit to the entire rotation curve: a halo component is always required.*

### 3.2 Dark Matter Theory

When faced with the preceding discussion of discrepancies between indirect mass measurements and luminosity observations, one is presented with two distinct conclusions to rectify the disagreement. One possibility is a change in the gravitational force law and the way in which objects react to the gravitational force, cf Bekenstein 2004, Brownstein & Moffat 2006 and Milgrom 1983. The other possibility is the presence of unseen matter. Solving this debate has been an active part of cosmological research. Concurrently, there has been no detection of dark matter in a laboratory. Indeed, the low level of electromagnetic interaction that dark matter would require to remain dark makes direct detection extremely difficult, if not impossible.

Within astrophysical contexts, there has been much work in settling this debate. One method includes obtaining mass density profiles of galaxies and galaxy clusters. Hoekstra et al. 2004 conducted a study of galaxy weak lensing and discuss their results in light of dark matter and alternative gravity theories. Hoekstra et al. 2004 find flattening of galaxy dark matter halos compared to the observed lens ellipticity. Further, the most prevalent alternative gravity theory, Modified Newtonian Dynam-

ics(MOND; cf Milgrom 1983), predicts an isotropic lensing result for galaxies on the scale used in this lensing study. Since anisotropic flattening was observed, Hoekstra et al. 2004 claim their study requires extra unseen matter, even when MOND is applied.

Additionally, Pointecouteau & Silk 2005 study x-ray data of galaxies clusters observed by the *XMM-Newton* satellite within the context of MOND and find a ratio of the dynamical mass in the MOND theory to the baryonic mass to be  $\frac{M_m}{M_b} = 4.94 \pm 0.50$ . According to Pointecouteau & Silk 2005, MOND still requires a dark component of mass to account for 80% of the mass at half of the virial radius.

Arguably one of the most convincing studies done in support of the dark matter hypothesis was done by Clowe et al. 2006. Here, the weak lensing observations and X-ray data from the *Chandra* x-ray satellite are combined to provide two independent reconstructions of the mass density of the Bullet Cluster, 1E 0657-558, which is undergoing a merger. Here, the weak lensing reveals two mass peaks separated by 0.72 Mpc. However, the x-ray data shows two mass concentrations much closer to each other. Since the mass reconstruction based on gravitational lensing is independent of the type of matter present, the reconstructed mass peaks separate from the baryonic mass concentrations are labeled by Clowe et al. 2006 as “direct empirical proof of the existence of dark matter”.

### 3.3 Dark Matter Halo Shape

#### 3.3.1 Shape Studies

As presented above, the dark matter theory has provided an explanation for astrophysical phenomena including mass to luminosity ratio discrepancies, galaxy rotation curves and lensing mass reconstructions showing separation of dark and baryonic matter. If one takes the standpoint that roughly one quarter of all mass-energy is

dark matter (cf Hinshaw et al. 2009), understanding its properties is crucial. While dark matter has not been directly detected in a laboratory, studies have been done to reconstruct dark matter mass distributions in astrophysical settings.

Early in the the study of dark matter halo shape, both theoretical and observational tests have shown halos to be non-spherical. An early example includes the work of Dubinski & Carlberg 1991. Using N-body simulations, Dubinski & Carlberg 1991 show the halos of galaxies to be triaxial and flat, with axial ratios of  $\langle s \equiv \frac{c}{a} \rangle = 0.5$  and  $\langle q \equiv \frac{b}{a} \rangle = 0.71$ , where a, b, and c represent the principal axis ratios of an ellipsoid, such that  $a \geq b \geq c$ . Additionally, the halos studied by Dubinski & Carlberg 1991 reproduce the observed rotation curves.

Allgood et al. 2006 study the dependence of dark matter halo shape on mass, redshift and radius. Here, virial masses range from  $9.0 * 10^{11} h^{-1} M_{\odot}$  to  $2.0 * 10^{14} h^{-1} M_{\odot}$ . Redshift varies from  $z = 0$  to  $z = 3$ . Allgood et al. 2006 find that the axial ratio, s, can be described by a simple power law,  $\langle s \rangle = (0.54 \pm 0.02) (\frac{M_{vir}}{M(z, \sigma_8)})^{-0.05 \pm 0.003}$ . Additionally, halo ellipticity displays Gaussian dispersion of 0.1 around the mean. Also, Allgood et al. 2006 demonstrate that the halo shape varies with radius, becoming more spherical at larger radii. However, the rate of change in ellipticity is more rapid in more massive halos.

### 3.3.2 Density Profiles

Throughout the study of dark matter halos, a few models have been proposed to analytically fit the shape of the density profiles. Perhaps the simplest well motivated model is the isothermal sphere, which would be expected of dark matter halos if violent relaxation were complete (cf Lynden-Bell 1967 and Shu 1977). The three-dimensional mass density associated with the singular isothermal sphere is

$$\rho(r) = \frac{\sigma^2}{2\pi G r^2}, \tag{3.7}$$

where  $\sigma$  is the one dimensional velocity dispersion. When projected along the line of sight, the convergence takes the simple form of

$$\kappa(\theta) = \frac{\theta_E}{2\theta}, \quad (3.8)$$

where  $\theta_E$  is the angular value of the Einstein radius for the deflecting mass. Making the isothermal sphere even more simple is the fact that the magnitude of the shear is equal to the convergence, since

$$\gamma = -\frac{\theta_E}{2\theta^3} (\theta_1^2 - \theta_2^2 + 2i\theta_1\theta_2). \quad (3.9)$$

Some recent observational studies have used the isothermal density profile. Treu & Koopmans 2002 found that the total mass within the Einstein radius of the lens galaxy D in MG2016+112 was well described by an isothermal density,  $\rho \propto r^{-2}$ . Rusin et al. 2003 studied 22 galaxy lens systems and found a density profile given by  $\rho \propto r^{-2.07}$ . Using weak lensing data collected as part of the Sloan Lens ACS Survey, Gavazzi et al. 2007 demonstrated a  $\rho \propto r^{-2}$  density profile out to  $300 \text{ h}^{-1} \text{ kpc}$ . All of these galaxies studies were of early type galaxies.

However, Wright & Brainerd 2000 state that the simplicity of the isothermal model might lead to its use “in order to obtain an estimate of the mass of a lens without fully reconstructing its true underlying density profile” (page 37). Within the isothermal model, the average shear at a given radius is proportional to the square of the velocity dispersion. Therefore, applying the isothermal sphere model gives the mass within a given radius, according to

$$M(r) = \frac{2\sigma^2 r}{G}. \quad (3.10)$$

Numerically, Navarro et al. 1996 use N-body simulations to construct dark matter halos of structures ranging from dwarf galaxies to galaxy clusters. The numerical

studies revealed density profiles that, at large radii, were approximately isothermal. However, the profile slope was much shallower than the  $r^{-2}$  trend of the isothermal sphere near the center. Also, near the virial radius, the slope becomes steeper than that of the isothermal sphere. The mass density profile associated with this work, generally referred to as the NFW profile, is given by

$$\rho(r) = \frac{\delta_c \rho_{cr}}{\left(\frac{r}{r_s}\right) \left(1 + \frac{r}{r_s}\right)^2}, \quad (3.11)$$

where  $r_s$  is the scale radius and  $\rho_{cr}$  is the critical density<sup>7</sup>.  $\delta_c$  is a density parameter,

$$\delta_c \equiv \frac{200}{3} \frac{c^3}{\ln(1+c) - \frac{c}{1+c}}, \quad (3.12)$$

where  $c$  is a concentration parameter given by

$$c \equiv \frac{r_{vir}}{r_s}. \quad (3.13)$$

It is worth noting that the original NFW profile, given by Equation (3.11) is spherically symmetric. As discussed above, realistic halos have been shown to be ellipsoidal. The NFW profile can be used in a triaxial context if radius is adapted to elliptical coordinates, e.g.

$$r \rightarrow R \equiv \sqrt{x^2 + \frac{y^2}{q^2} + \frac{z^2}{s^2}}. \quad (3.14)$$

In this system, the largest principal axis is placed along the x-axis, the second largest is along the y-axis and the smallest is along the z-axis. Parameters  $q$  and  $s$  represent the principal axis lengths in each corresponding direction, as a fraction of the semi-major axis length.

Convergence and shear of the NFW profile take on more complicated forms an-

---

<sup>7</sup>This is the *cosmological* critical density,  $\rho_{cr} = \frac{3H^2}{8\pi G}$ , where  $H$  is Hubble's Constant.

alytically than the isothermal sphere (cf Bartelmann 1996 and Wright & Brainerd 2000).

$$\kappa(r) = \frac{2\delta_c \rho_{cr} r_s}{\Sigma_{cr} \left( \frac{r^2}{r_s^2} - 1 \right)} f \left( \frac{r}{r_s} \right), \quad (3.15)$$

where

$$f(x) \equiv \begin{cases} 1 - \frac{2}{\sqrt{x^2 - 1}} \arctan \sqrt{\frac{x-1}{x+1}}, & x > 1 \\ 1 - \frac{2}{\sqrt{1-x^2}} \operatorname{arctanh} \sqrt{\frac{1-x}{1+x}}, & x < 1 \end{cases}. \quad (3.16)$$

### 3.4 Mass Reconstruction Methods

Understanding observational techniques is necessary to demonstrate how the shear map influences how well mass densities can be reconstructed from a practical standpoint. In order to understand how mass densities are inferred observationally, two methods of determining dark matter halo shape and density are listed in this section. These observational methods use measurements of galaxy ellipticity to map the shear of the lensing system, which is then used to infer either the mass distribution itself or ellipticity parameters of the mass distribution.

One method of reconstructing the mass density of a dark matter halo was outlined by Kaiser & Squires 1993. This method relates the surface mass density to the ellipticity of background galaxies. Once background galaxies have been identified, the quadrupole moments of the images are calculated according to

$$Q_{ij} = \int \mathcal{I}(\theta) \theta_i \theta_j d^2\theta, \quad (3.17)$$

where  $\mathcal{I}(\theta)$  is the surface brightness of the image. Kaiser & Squires 1993 give the ellipticity, as a polar quantity in Cartesian coordinates,  $(x_1, x_2)$ , as

$$\begin{pmatrix} e_1 \\ e_2 \end{pmatrix}_S = \begin{bmatrix} \frac{(Q_{11}-Q_{22})}{(Q_{11}+Q_{22})} \\ \frac{2Q_{12}}{Q_{11}+Q_{22}} \end{bmatrix}. \quad (3.18)$$

Equation (3.18) was obtained in the reference frame where the quadrupole moment tensor is diagonal. This relationship will be related back to general coordinates below. The subscript,  $S$ , is used here to represent the unlensed, source frame of reference. The altered ellipticities become

$$\begin{pmatrix} e_1 \\ e_2 \end{pmatrix}_L = \begin{pmatrix} e_1 \\ e_2 \end{pmatrix}_S + \left( \frac{\partial^2 \psi}{\partial \theta_2^2} - \frac{\partial^2 \psi}{\partial \theta_1^2} \right) \begin{pmatrix} 1 - e_1^2 \\ e_1 e_2 \end{pmatrix}_S, \quad (3.19)$$

up to first order. The next part of the reconstruction takes advantage of averages of galaxy ellipticities. It is assumed that galaxies are distributed randomly, so that

$$\langle e_1 \rangle_S = \langle e_2 \rangle_S = \langle e_1 e_2 \rangle_S = 0. \quad (3.20)$$

However,  $\langle e^2 \rangle$  is non-zero, leading to

$$\langle e_1 \rangle_L = \left( \frac{\partial^2 \psi}{\partial \theta_2^2} - \frac{\partial^2 \psi}{\partial \theta_1^2} \right), \quad (3.21)$$

since the factor of  $1 - \frac{\langle e^2 \rangle}{2} \approx 1$ , according to Kaiser & Squires 1993 (page 442).

Thus, the ellipticity can be related to the lensing potential. In general coordinates, the ellipticity becomes

$$\begin{pmatrix} e_1 \\ e_2 \end{pmatrix}_L = \begin{bmatrix} \frac{\partial^2 \psi}{\partial \theta_1^2} - \frac{\partial^2 \psi}{\partial \theta_2^2} \\ 2 \frac{\partial^2 \psi}{\partial \theta_1 \partial \theta_2} \end{bmatrix}. \quad (3.22)$$

Using Equation (2.11), Kaiser & Squires 1993 then relate the ellipticity to the mass density, by solving the partial differential equations in Fourier space<sup>8</sup>.

---

<sup>8</sup>This is the reverse procedure presented here in Section 5.1 for the calculation of shear. However, Kaiser & Squires 1993 use the notation,  $e$ , for ellipticity, which is  $2\gamma$  in the notation presented here. This is a non-traditional representation of ellipticity, which is generally defined as  $e = 1 - \frac{b}{a}$ , where  $a$  and  $b$  are the semi-major and semi-minor axis lengths, respectively.

One example of the application of the Kaiser & Squires 1993 method is the reconstruction of the merging cluster 1E0657-558 by Clowe et al. 2004. However, in this study the galaxy ellipticities were used to find the reduced shear,

$$g = \frac{\gamma}{1 - \kappa}. \quad (3.23)$$

To apply this measurement to the Kaiser & Squires 1993 method, Clowe et al. 2004, start with an simple uniform convergence and iteratively refine the reduced shear measurement to obtain the convergence of the lensing mass, relative to the value of the convergence at the edge.

Natarajan & Refregier 2000 present a method of obtaining the mass and ellipticity of a lens galaxy through galaxy-galaxy lensing. For a given convergence and appropriate weight function,  $w(\theta)$ , such that

$$M = \int w(\theta)\kappa(\vec{\theta})d^2\theta, \quad (3.24)$$

Natarajan & Refregier 2000 define quadrupole moments

$$Q_{ij} = \int w(\theta)\kappa(\vec{\theta})\theta_i\theta_jd^2\theta. \quad (3.25)$$

Ellipticity is then defined as

$$\epsilon \equiv \frac{Q_{11} - Q_{22} + 2iQ_{12}}{Q_{11} + Q_{22}}. \quad (3.26)$$

To relate these quantities to the measured shear values, Natarajan & Refregier 2000 use the quadrupole-shear relationships found by Schneider & Bartelmann 1997,

$$Q = \int \left( g_t(\theta)\gamma_t(\vec{\theta}) + ig_\times(\theta)\gamma_\times(\vec{\theta}) \right) e^{-2i\phi}d^2\theta, \quad (3.27)$$

where  $\phi$  is the coordinate angle,  $t$  and  $\times$  represent the tangential and cross components (cf Equations (2.26) and (2.27)), and

$$g_t(\theta) = 2V_2(\theta) - \theta^2 w(\theta) \quad (3.28)$$

$$g_\times(\theta) = -2V_2(\theta), \quad (3.29)$$

and  $V_n(\theta) = \frac{1}{\theta^2} \int_0^\theta \theta'^{n+1} w(\theta') d\theta'$ . With these definitions, Natarajan & Refregier 2000 obtain the lens ellipticity,  $\epsilon$ , with

$$T = \int g_t(\theta) \gamma_t(\vec{\theta}) d^2\theta \quad (3.30)$$

$$M = \int h_t(\theta) \gamma_t(\vec{\theta}) d^2\theta, \quad (3.31)$$

where  $h_t(\theta) \equiv 2V_0(\theta) - w(\theta)$ . Natarajan & Refregier 2000 then apply this method to the (elliptical) isothermal model to demonstrate the effectiveness of this method with data from the Sloan Digital Sky Survey.

Both of these observational methods rely on establishing shear values based on image ellipticities. Shear maps are then used to reconstruct mass distributions. Each observational method includes sources of noise. Both error introduced through astronomy, such as atmospheric distortion, and systematic error in reconstruction methods account for inaccuracies in mass reconstruction. In light of demonstrations of dispersion in the mass density itself, it would be helpful to understand what influence variations in mass density have on shear. Statistics of mass density dispersion effects on shear can help separate these variations from noise.

## 4 Deflection Angle Calculation and Ray Tracing

### 4.1 Usefulness of Deflection Angle Calculations

Ray tracing provides a simple method of simulating gravitational lensing, albeit computationally intensive. Images of background sources may be produced graphically, providing a visualization for what could possibly seem like arbitrary mathematical results. Additionally, the shear calculation method presented in Section 5 fails in the strong lensing regime, where the ray trace method excels.

Deflection angles provide an alternative method of finding critical curves and shear. The transformation matrix,  $A$ , as defined in Equation (2.16), can be redefined in terms of the scaled deflection angle,  $\alpha$ , according to

$$A = \begin{bmatrix} 1 - \frac{\partial \alpha_1}{\partial x_1} & -\frac{\partial \alpha_1}{\partial x_2} \\ -\frac{\partial \alpha_2}{\partial x_1} & 1 - \frac{\partial \alpha_2}{\partial x_2} \end{bmatrix}. \quad (4.1)$$

Using this definition, shear may be related to the deflection angle by

$$\gamma_1 = \frac{1}{2} \left( \frac{\partial \alpha_1}{\partial x_1} - \frac{\partial \alpha_2}{\partial x_2} \right) \quad (4.2)$$

$$\gamma_2 = \frac{\partial \alpha_1}{\partial x_2} = \frac{\partial \alpha_2}{\partial x_1}. \quad (4.3)$$

Finally, using the trace of the transformation matrix, one can also calculate convergence,

$$\kappa = \frac{1}{2} \left( \frac{\partial \alpha_1}{\partial x_1} + \frac{\partial \alpha_2}{\partial x_2} \right). \quad (4.4)$$

### 4.2 Procedure

In most numerical calculations pertaining to galaxy and galaxy cluster mass distributions, mass is treated as a distribution of particles<sup>9</sup>. Discretization of mass allows

---

<sup>9</sup>For a discussion on the generation of such mass distributions, see Appendix A.

mathematically complex functions, often not analytical, to be simplified. In the case of deflection angles, the contribution of each particle to the overall bending angle at any point can be approximated to that of a point particle, given by Equation (2.1), applying particle smoothing if resolution and accuracy require it. This simplification provides the means to calculate deflection angles for arbitrary mass distributions by simply summing over each particle's contribution.

While deflection angles can be calculated at any point for a list of particles in a mass distribution, typically they are calculated on a grid with arbitrary resolution. It is not necessary to place the mass distribution on a discrete grid when performing a summation. However, since the mass densities are also used in convolution shear studies (cf Section 5.1), the grid method is used for deflection angle calculations as well. The resolution can be adjusted along with particle smoothing for desired precision. At this point, it is worth noting that other ray-trace methods are in use that calculate the deflection angles using the fast Fourier transform method. With this calculation method, a grid is required. Indeed, with a larger set of particles, this method would provide a calculation speed increase, which was achieved here through parallelization. An example of ray-tracing using fast Fourier transform is Jain et al. 2000, although these authors use ray-tracing to calculate shear, not deflection angle. Additionally, Aubert et al. 2007 use a summation method to calculate deflection angle, as well as convergence, shear and potential. Here, the contribution of each particle is summed individually, with a smoothing factor. To overcome CPU limitations, these authors use a tree decomposition technique, where the two-dimensional distribution of particles is divided into sub-regions, whose overall effect is determined based on distance.

Figure 4.1 shows the general class structure of the ray trace program that was created for this study. All two-dimensional data is contained in a template class called *Plane*, simplifying the handling of double arrays. Data consists of two types, *Double*,

which is a custom wrapper for the double type and *Complex*, which is an object containing two double type variables, representing a complex number. These wrapper classes were created as a simple way of manipulating two and three-dimensional variables, as well as color information for pixels of images produced by ray-tracing. All mass functions are contained in the *DensityProfile* object. Main deflection angle and ray-trace calculations are performed by the *GLAlgorithm* object. The main program then simply references *GLAlgorithm* for each point in the lensing plane. Deflection angles are stored as *Complex* objects, using the orthogonality of complex numbers as a basis for two-dimensional vectors. After the calculation is performed, the grid values can be stored as a data file or drawn as a bitmap, using the methods contained in the *Plane* object. To trace the light rays back to source plane locations, *GLAlgorithm* simply alters the original source position by the deflection angle according to Equation (2.8).

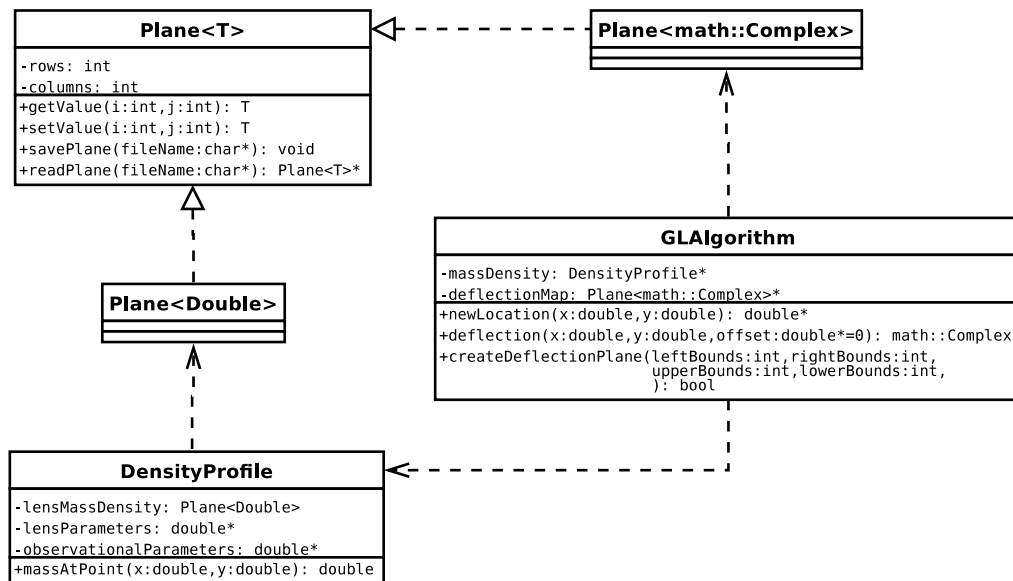


Figure 4.1: Ray Trace Class Diagram

For each point on the grid, the deflection angle is calculated, treating each particle as a point mass. Immediately, one sees that this method is computationally intensive, most notably in CPU time as computation is  $\mathcal{O}(N_{particle}^2 * N_{point}^2)$ . However, the

discretization that allows this calculation to take place also easily lends itself to parallel computing. By dividing the mass density into subsections, calculations can be performed on an arbitrary number of computers simultaneously, recombining the results later.

### 4.3 Volunteer Computing: BRaTS@Home

To carry out parallel computing for this study, the BRaTS@Home Distributing Computing was created in 2007. As the recursive acronym, BRaTS Ray Trace Simulation at Home, implies, BRaTS@Home distributes these discrete deflection angle calculations to computers provided by volunteers via the internet. With 190 users in at least twenty-nine countries, as of April 2010, BRaTS@Home provides a several hundred computer node cluster, as most users provided multiple computers, including dual and quad core machines.

On a Pentium III PC running the Ubuntu distribution of Linux, BRaTS@Home runs the BOINC<sup>10</sup> server system, an open source derivative of the SETI@Home project (Anderson 2004). These calculations are carried out using the idle time processes generally devoted only to screen savers. Volunteers' computers, or clients, download mass distribution data and ray-tracing software from the BRaTS@Home server and upload the results via an automated CGI program. On the client, a BOINC program monitors the CPU and memory usage of the scientific programs. With this client software, the user can dictate how much processor time is dedicated to the scientific programs, varying the noticeable effects the scientific software has on the computer, if any. Using the C++ API, an intermediate program, known as a wrapper, was written for the clients. By using a wrapper program, the scientific application for calculation deflection angles can be left unchanged, placing all of the necessary BOINC routines needed by the client, such as progress notification, in the wrapper. The organization

---

<sup>10</sup>Berkeley Open Infrastructure for Network Computing

and operational layout of the BOINC system is illustrated in Figure 4.2.

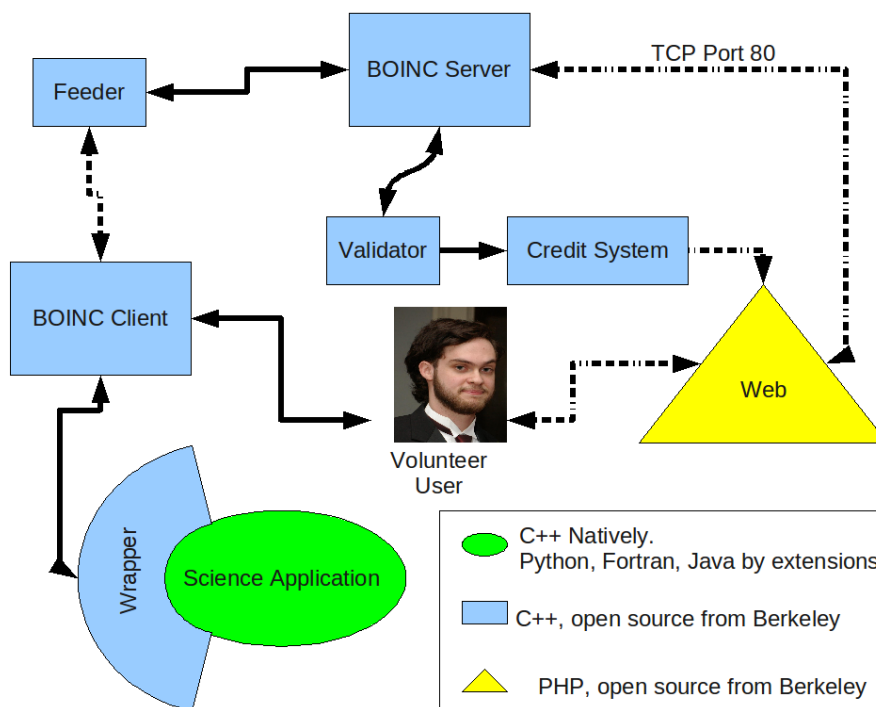


Figure 4.2: Organizational Diagram for the BOINC System BRaTS@Home

Volunteer computing has benefits for both scientists and general public. For scientists, a parallel computing cluster can be setup for the costs of one server, since volunteer computers are being used. The international community of nearly two million people<sup>11</sup> have provided an average of 4 hosts per person. Another benefit for scientists is bringing their work to the general public. Project websites include message boards for discussion between project scientists and those volunteering computer time. Some project scientists post links to papers and provide descriptions of their work in language applicable to general audience, something easily neglected in specialized fields. Additionally, BRaTS@Home has conducted a live on-line science discussion.

For volunteers there are reasons to donate computer time. As previously men-

<sup>11</sup>As of April 2010, according to boincstats.com, a compilation of projects' user data.

tioned, volunteers are now involved in scientific causes that are already familiar, such as climate change<sup>12</sup> (Myles 1999), or topics that are less familiar, such as protein structure analysis<sup>13</sup> (Qian et al. 2007).

Another driving force behind participation is recognition and competition. Credits are assigned to participants based on CPU usage, in units known as cobblestones. With these credits participants compete to obtain the most units, both individually and on teams.

#### 4.4 Impact of Distributed Computing

Parallel computing provides a net processing speed benefit, as multiple independent computations are performed simultaneously. In an attempt to quantify the impact parallel computing on this study, processing and user statistics are provided in Table 4.1. For comparison, the same data is listed for the general BOINC community, using data retrieved from the online BOINC statistics service, boincstats.com, which routinely collects data directly from BOINC projects. The statistics provided in this section are up-to-date as of April 11, 2010, after which no further work was done using the BRaTS@Home project.

BRaTS@Home was brought on-line on June 5, 2007 and the first simulation was run on the following day. Within this time period, the combined CPU usage of all of the client computers was 278.28 days. The simulation grids, as described in Section 4.2, were divided into equal subsections, totaling either four or sixteen subsections, depending on the total number of non-zero mass points of the lens for each particular work unit. For comparison, it should be noted that when no parallelization was used, these ray-trace simulations had an average run-time of seven hours on the computer that serves as the host for the project. Through the use of parallel computing, complete data sets can be calculated in roughly one hour.

---

<sup>12</sup>climateprediction.net

<sup>13</sup>Rosetta@home

Computation time scales as  $\mathcal{O}(N_{mass}^2 * N_{ray}^2)$ , where  $N_{mass}$  represents the number of points in the mass grid and  $N_{ray}$  represents the number of points to be ray-traced. The subsections that one particular volunteer would ray-trace represented a unique subsection of  $N_{ray}$ , while all volunteers used the entire mass grid. For example, if a 512x512 square pixel grid was divided into 16 subsections, each volunteer would ray-trace  $128 * 128 = 16384$  different points, summing over  $512 * 512 = 262144$  points in mass grid for each of the 16384 ray-trace points. Since the end result is a linear superposition of the deflection angles due to each of the points in the mass grid, it is possible to subdivide the mass grid as well. However, the performance gain resulting from subdividing the ray-trace grid,  $N_{ray}$ , was sufficient for this project. If a larger speed improvement was needed, i.e. if resolution is improved, the mass grid should be subdivided as well.

When one compares the CPU usage in Table 4.1 with the run-time of one entire ray-trace simulation, the benefit of parallelization becomes clear. The combined CPU usage amounts to 278.28 days, which is based on the recorded times of each particular client computer. Computation speed varies inversely with the number of subsections when the parallelization is used as described above. Therefore, the impact on CPU time proved by the project is profound.

Additionally, projects such as BRaTS@Home provide an excellent platform to bring science to the general public. As shown in Table 4.1, more than 115 volunteer users have participated in the project, representing people from various backgrounds. The total number of users exposed to the science behind the project is larger, since some users did not run simulations due to the number of simulations run compared to the number of users enrolled. In fact, the total number of users enrolled in the project is 190. All users enrolled in the project have the ability to discuss the project using the on-line message board. Additionally, a live on-line discussion of the science behind the project was held on January 23, 2010. While not all participants are

active in on-line discussion, the potential to reach a large audience of various levels of science understanding is present. Among participants who voluntarily state their country of origin, 29 countries are represented at BRaTS@Home. As shown in Table 4.1, the whole BOINC community represents almost ten times as many countries and a four order of magnitude increase in registered users, compared to BRaTS@Home.

	BRaTS@Home	All BOINC projects <sup>14</sup>
Combined CPU usage	278.28 days	Unknown
Average credit per CPU second	0.0035	Unknown
Total credit granted <sup>15</sup>	76709.26	$2.14 * 10^{11}$
Total number of users <sup>16</sup>	115	$1.9 * 10^6$
Total identified countries	29	267
Total number of teams	62	86925

Table 4.1: BRaTS@Home and overall BOINC Statistics as of April 11, 2010

## 4.5 Verification of Accuracy

Whenever numerical simulations are used, it is necessary to verify whether or not the results agree with expected values, either theoretical or experimental. Here, uniform ellipses are used as a test case, since the deflection angle of the uniform ellipse is known analytically. In this case, ellipses have a constant density, with a total mass,  $M$ , and semi-major and semi-minor lengths of  $a$  and  $b$ , respectively. Schramm 1990 showed that confocal to this deflecting mass are ellipses of equal deflection angle given

<sup>14</sup>Last retrieved from boincstats.com on April 11, 2010.

<sup>15</sup>Based on CPU credit, which differs slightly from user credit, due to credit granted during the testing phase.

<sup>16</sup>Total including only those receiving work for which credit was granted.

by

$$\alpha_x = -\frac{8GMx}{c^2a'(a'+b')} \quad (4.5)$$

$$\alpha_y = -\frac{8GMb}{c^2b'(a'+b')} \quad (4.6)$$

outside of the mass, where  $a'^2 = a^2 + \lambda$ ,  $b'^2 = b^2 + \lambda$  and outside of the mass distribution  $\lambda > 0$ . Within the elliptical mass, Equations (4.5) and (4.5) can be used if the primed variables are replaced with corresponding unprimed variables, i.e.  $\lambda \rightarrow 0$ . The numerical results for the circular case is given in Figure 4.3.

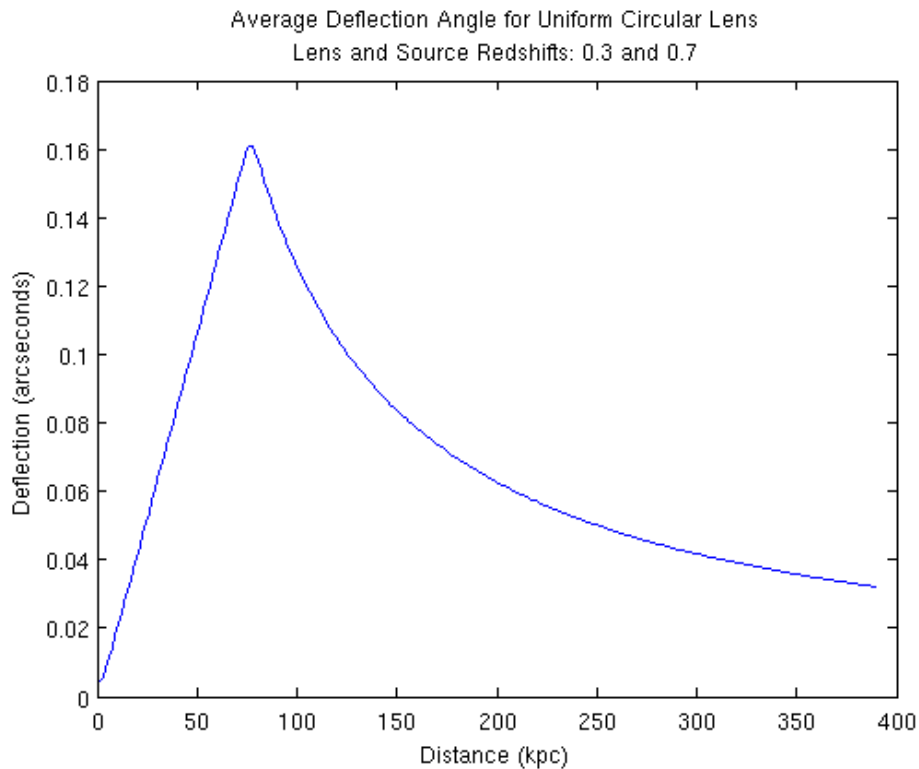


Figure 4.3: Deflection angle for a  $3 * 10^{11} M_{\odot}$  circular lens.

For comparison, deflection angles were calculated via ray tracing by BRaTS@Home and analytically for uniform elliptical deflecting masses using the results of Schramm 1990. Table 4.2 shows the ratio of the numerical results to the analytical results for various axis ratios. Axis ratios are the ratio of the semi-minor to semi-major axes,

where a ratio of one corresponds to a circle. Each distribution has a total mass of  $3 * 10^{11} M_{\odot}$ , spread out uniformly within the ellipse. In each case, values are on average within two percent of the analytical value. In the worst scenario, the 0.1 axis ratio ellipse, all points are within ten percent. On the other hand, the best results are given by the circular lens, where all points are within 2.39% of the actual value.

Axis Ratio	Deflection Angle Ratio			
	Average	Minimum	Maximum	Standard Deviation
0.1	0.9847	0.9038	1.0510	0.0037
0.3	0.9848	0.9605	1.0110	0.0010
0.5	0.9848	0.9720	0.9983	0.00053
1.0	0.9849	0.9761	0.9924	0.00034

Table 4.2: Numerical and Analytical Deflection Angle Comparison

## 5 Numerical Calculation of Shear

### 5.1 Calculation of Shear via Convolution of Convergence

As shown in Section 2.2, both convergence and shear are related to the lensing potential through a combination of second derivatives,

$$\kappa(x_1, x_2) = \frac{1}{2} \nabla^2 \psi \quad (5.1)$$

$$\gamma_1(x_1, x_2) = \frac{1}{2} \left( \frac{\partial^2 \psi}{\partial x_1^2} - \frac{\partial^2 \psi}{\partial x_2^2} \right) \quad (5.2)$$

$$\gamma_2(x_1, x_2) = \frac{\partial^2 \psi}{\partial x_1 \partial x_2} . \quad (5.3)$$

While solving these partial differential equations might be possible for simple mass distributions, a realistic shear study requires calculations for arbitrary mass distributions. Performing the differentiation in Fourier space simplifies the mathematics that relate mass density, through convergence, to shear. This can be seen by defining the lensing potential in terms of a Fourier transform,

$$\psi(x_1, x_2) \equiv \frac{1}{2\pi} \int \tilde{\psi}(k_1, k_2) e^{-i\vec{k} \cdot \vec{x}} d^2 k . \quad (5.4)$$

Using this definition of the potential, only the exponential function in the integrand contains the real space coordinates,  $x_1$  and  $x_2$ . Therefore, differentiation in Fourier space simply results in multiplication by Fourier conjugates and appropriate factors of the imaginary number. Thus, in Fourier space, the complex shear,  $\gamma = \gamma_1 + i\gamma_2$ , can be related to the convergence by

$$\tilde{\gamma}(k_1, k_2) = \tilde{\kappa}(k_1, k_2) \frac{k_1^2 - k_2^2 + 2ik_1 k_2}{k_1^2 + k_2^2} . \quad (5.5)$$

Using the fast Fourier transform routine (Press et al. 1992), shear can be calculated numerically for a given mass density.

## 5.2 Shear Calculation

The first requirement is a two-dimensional projection of the mass density. Three-dimensional matter distributions are simulated by distributing a collection of particles of equal mass according to the required mass density. For a detailed description of the process of distributing particles, see Appendix A. The two-dimensional projection is made by dividing the three dimensional space into a set of columns along the desired line of sight. The widths of the columns perpendicular to the line of sight is adjusted for the necessary resolution. The total mass of all of the particles in each column is then retained as the total mass within the corresponding portion of the two-dimensional projection. This projection procedure is repeated for each column in the mass distribution. Dividing this mass distribution by the area of each grid point, i.e. column cross-section, and the critical density,  $\Sigma_{cr}$ , gives the convergence for the mass distribution. Figure 5.1 shows a projected convergence (on a log scale) for a simulated triaxial NFW distribution. Here, the line of sight was taken to be at azimuthal and polar angles of  $45^\circ$  with respect to the longest principal axis of the distribution.

Once the convergence has been calculated, the Fourier transform of the convergence is calculated using the Fast Fourier Transform (FFT) routine. A thorough explanation on the implementation of FFT is provided by Press et al. 1992. Each element in the resulting Fourier transform of the convergence is then multiplied by the corresponding factor of differentiation, according to Equation (5.5), to obtain the Fourier transform of the shear. Inverse Fourier transformation of the result then gives the shear for the two-dimensional grid provided by the convergence.

The FFT calculation method presented here is exactly like that of the mass recon-

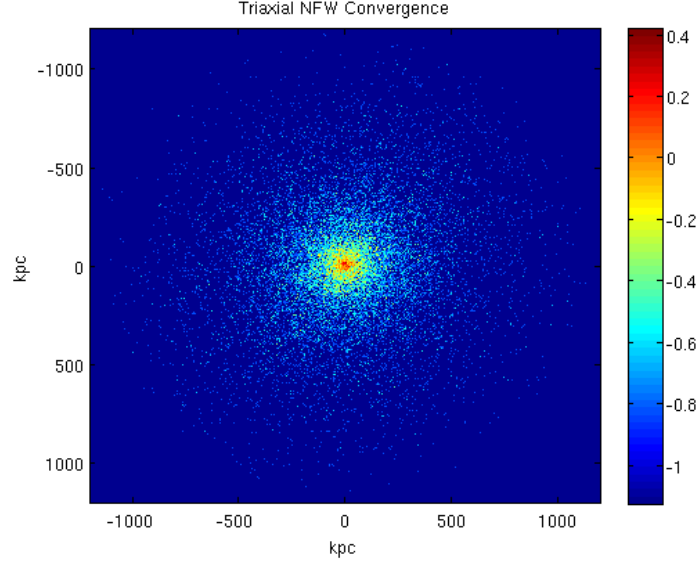


Figure 5.1: Simulated triaxial NFW distribution with lens (source) redshift of  $z = 0.3$  (0.7).  $M_{vir} = 2 * 10^{14} h^{-1} M_{\odot}$ ,  $R_{vir} = 1200 h^{-1} kpc$ ,  $c = 4.8$ ,  $q = 0.8$ ,  $s = 0.5$  and semi-major axis is placed along  $\theta = \phi = \frac{\pi}{4}$  using a log scale.

struction method generally referred to as Kaiser-Squires Inversion (Kaiser & Squires 1993). In fact, Kaiser-Squires Inversion follows this procedure in reverse, to calculate the convergence from shear values. This method is not without its drawbacks (cf Schneider et al. 2006, page 317). Some of these difficulties include: loss of shear information due to estimation based on smoothing of galaxy images, integration over a finite grid instead of an infinite plane (i.e.  $\mathbb{R}^2$ ), and the so-called mass-sheet degeneracy problem. However, in the simulations performed here, the actual convergence value is known, within provided resolution, eliminating most of these problems, including the mass-sheet degeneracy problem. This problem stems from the fact that a known convergence value belongs to a class of convergences, for which the same image ellipticities would be observed. For any convergence,  $\kappa(\vec{\theta})$ , there is a set of convergences,  $\kappa_{\lambda}(\vec{\theta}) = 1 - \lambda (1 - \kappa(\vec{\theta}))$ , for any value of  $\lambda$ . For each  $\lambda$ , the shear would be transformed by  $\gamma_{\lambda}(\vec{\theta}) = \lambda \gamma(\vec{\theta})$ . However, reduced shear and the axis ratios of the images produced by this class of lenses remain unchanged for all values of  $\lambda$ , as can be seen by Equations (2.25) and (3.23). While observational reconstructions begin with

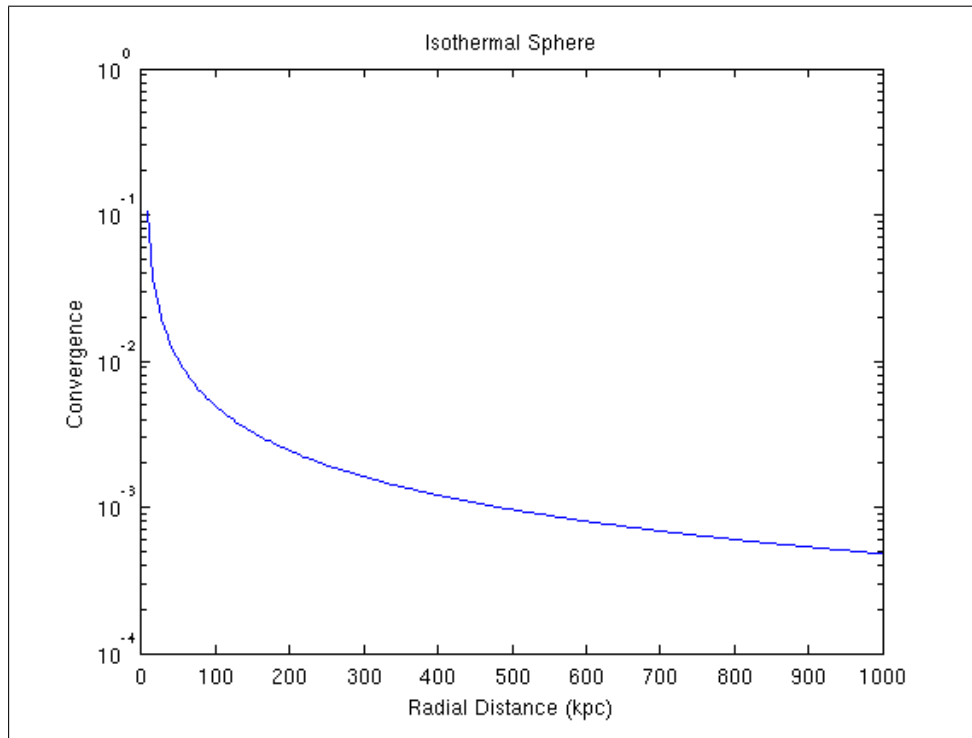
measurements of image ellipticity, a function of axis ratios, the shear calculations here begin with convergence maps themselves. Therefore, although the procedure followed here is similar to Kaiser-Squires mass reconstruction, this problem is not introduced. Indeed, the main source of error here are the limitations of resolution of the convergence. This effect is quantified in Section 5.3.

### 5.3 Comparisons with Analytical Solutions

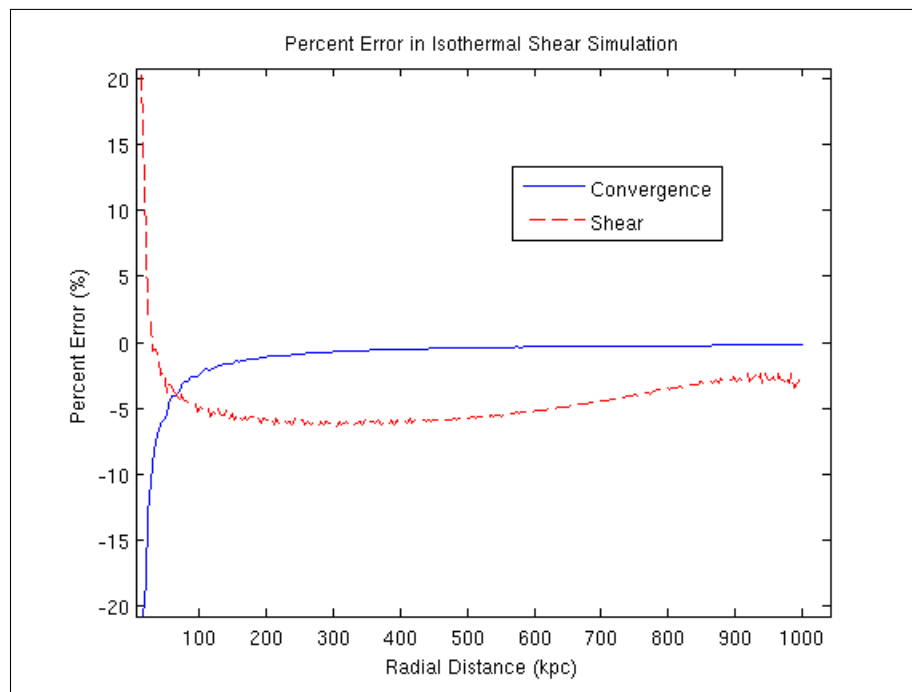
To understand the limitations of shear calculations presented here, mass distributions are tested for which analytical results are known, with the end goal of having a reliable method of shear calculation for arbitrary mass distributions, for which shear cannot be calculated analytically.

The first distribution so tested is the isothermal sphere, discussed in Section 3.3.2. For this test case, a two-dimensional convergence map was calculated analytically for a 512-by-512 grid, according to Equation (3.8). The length of the grid in each direction is  $1 \text{ h}^{-1} \text{ Mpc}$  and the points in the grid are evenly spaced. The lens was placed at a redshift of 0.35 and background sources are located at  $z = 0.8$ . For this particular lens, the Einstein radius, which is a function of the velocity dispersion, is taken to be  $0.96 \text{ h}^{-1} \text{ kpc}$  to keep calculated points in the weak lensing regime. Additionally, these parameters were used by Lasky & Fluke 2009, providing a comparison with an example already used in literature. Using this convergence grid, shear was calculated via FFT convolution. For comparison with the analytical values, the values of the shear and convergence are averaged over radial values spanning the entire distribution. Figure 5.2(a) shows the convergence profile. As a measurement of error, the percent difference of the shear was calculated according to  $100 * \left(1 - \frac{\text{Simulation}}{\text{AnalyticalValue}}\right)$ .

Near the center of the grid, the shear values diverge, as does the convergence, though in different directions. Analytically, shear and convergence diverge near the origin. While one would expect a numerical simulation to begin to fail in regions



(a) Isothermal Sphere Convergence



(b) Percent Error for Isothermal Sphere Shear

Figure 5.2: Isothermal sphere located at  $z = 0.35$ , with background sources at  $z = 0.8$ , with an Einstein radius of  $0.97 h^{-1} \text{ kpc}$ .

where the analytical results diverge, grid based calculations such as these are known to be inappropriate in regions of strong lensing and other methods should be used (cf Aubert et al. 2007). Outside of this region, there is a systematic over-estimation, within 5% of the analytical value.

While the isothermal sphere provides an analytical result against which comparisons can be made, its spherical symmetry and analytical convergence map is less similar to the mass distributions which are to be studied as the goal of this work. Therefore, the next test to be performed is for the triaxial NFW halo. This distribution has been shown to resemble realistic dark matter halos, cf Section 3.3.2. Simulated cluster halos are created as a three-dimensional distribution, which will be projected onto two-dimensional convergence maps. This projection procedure is also used in the NFW comparison.

As the NFW profile is more complex than the isothermal sphere model, the convergence and shear values take a more complicated analytical form. However, shear and convergence for the triaxial NFW profile can be calculated through numerical integration, using the procedure described in Appendix B.

For this comparison, the mass distribution has a virial mass of  $2 * 10^{14} h^{-1} M_{\odot}$  and a virial radius of  $1200 h^{-1} kpc$ . The concentration is equal to 4.8. The principal axis runs along azimuthal and polar angles of  $45^{\circ}$  with respect an axis perpendicular to the line of sight. The axial ratios  $q$  and  $s$  are 0.8 and 0.5, respectively. With these parameters, a three dimensional distribution with 135000 particles was created. This distribution was then projected onto a convergence map, shown in Figure 5.1.

With this convergence map, shear is calculated by FFT convolution. The shear and convergence values are averaged over circles of varying radii centered around the origin. Averaging over radius reveals the overall profile of the cluster. Although the distribution is ellipsoidal, circular average bins are used for continuity with observational practices. Expected values of the shear and convergence are calculated

by numerical integration. For each radius used in the averaging of simulation values, twenty shear values at points of equal distance from the center are calculated by numerical integration over a complete circle, using evenly spaced azimuthal angles. After calculating the shear and convergence profiles by simulation and numerical integration, the percent difference was calculated, shown in Figure 5.3.

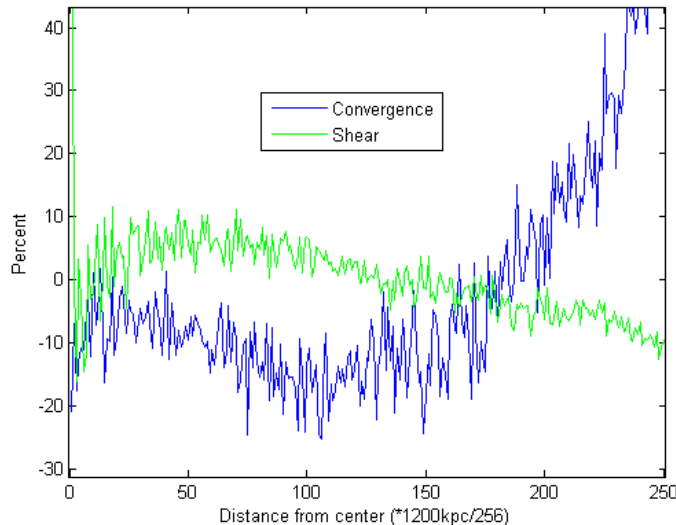


Figure 5.3: Percent error for triaxial nfw convergence and FFT-calculated shear, compared to values found through numerical integration. Radial distance extends to the virial radius.

Figure 5.3 shows the simulated profile tends to overestimate the convergence values of the mass distribution, within roughly two-thirds of the virial radius, corresponding to an underestimation of shear. For distances greater than  $\frac{2}{3}R_{vir}$ , the simulated convergence becomes less than the expected value. When averaged over the virial radius, the percent difference of the convergence approaches zero. Within a distance of  $0.5R_{vir}$  from the center, the average percent error of the FFT calculated shear is 5%, equaling the error outside of  $0.5R_{vir}$  in magnitude, but differing in direction of inaccuracy.

## 6 Correlation Study of Mass Ellipticity and Shear

### 6.1 Galaxy Cluster Distributions

Dark matter halo shape within the cold dark matter theory has been examined in recent years. It has been shown that, although there is a correlation between halo mass and ellipticity, there is dispersion about the mean ellipticity, so that there is a range of ellipticities for a given halo mass (cf Allgood et al. 2006). While these studies have been done theoretically, reconstructing galaxy and galaxy cluster mass densities is an active part of astrophysics. As resolution and field of view of such observations improve, it becomes increasingly important to understand what effect this dispersion has on measured shear values.

To study this effect, shear maps are created for seven simulated dark matter halos. For each of these distributions, mutually perpendicular lines of sight are examined. Thus, twenty-one shear maps are produced from different convergences. The parameters for the clusters are provided in Table 6.1. Mass distributions labeled 5, 7, 9, 10, 11 and 14 are high-resolution Adaptive Refinement Tree (ART) N-body simulations of clusters, while distribution 24 is a group undergoing a merger. These seven distributions correspond to the distributions used by Flores et al. 2007 to study the statistics of dark matter halo shapes with respect to x-ray observations. Quantities  $c$ ,  $q$  and  $s$  listed in Table 6.1 correspond to the NFW parameters used in Section 3.3.2 and were found by dividing the mass distribution into isodensity shells. From these shells, the ellipticity can be deduced. It is worth noting that the ellipticity varies with radial distance.

To produce the shear maps, each of the mass distributions are projected perpendicular to three orthogonal lines of sight. The resulting convergence map extends to the virial radius of the distribution. The mass distributions are characterized by a triaxial ellipsoidal shape, as shown in Table 6.1. The orientation of the longest

Cluster	$M_{vir}(10^{14} h^{-1} M_{\odot})$	$R_{vir} (h^{-1} kpc)$	$R_s(h^{-1} kpc)$	c	q	s
5	2.33	1550	170	9.1	0.777	0.623
7	2.38	1562.31	173.59	9	0.610	0.466
9	1.42	1313.62	154.54	8.5	0.481	0.381
10	0.991	1166.57	137.24	8.5	0.626	0.431
11	1.20	1243.31	126.9	9.8	0.617	0.464
14	1.25	1259.81	143.16	8.8	0.513	0.417
24	0.690	1034.01	114.89	9	0.413	0.404

Table 6.1: Simulated Cluster Data

principal axis with respect to the line of sight is listed in Table 6.2 for each projection of each cluster. Once the convergence has been obtained, the shear is calculated for each line of sight. Table 6.3 provides the resolution data for each cluster. Each cluster is bounded by its virial radius. All clusters are placed at a redshift of  $z = 0.2$ , which corresponds to an angular diameter distance of  $D_L = 671.89 h^{-1} Mpc$ . Each cluster's particles are projected onto a 512-by-512 grid perpendicular to the line of sight, with resolutions listed in Table 6.3.

Cluster	Line of Sight	$\theta$ (radians)	$\phi$ (radians)
5	X	1.641	0.611
5	Y	0.646	1.937
5	Z	-0.733	1.100
7	X	2.862	0.524
7	Y	-1.100	1.868
7	Z	0.611	1.222
9	X	1.990	1.274
9	Y	-0.401	0.384
9	Z	0.489	1.815
10	X	-1.658	0.646
10	Y	-0.244	1.693
10	Z	1.222	0.942
11	X	0.716	0.559
11	Y	-0.175	1.455
11	Z	1.571	1.972
14	X	-2.618	0.785
14	Y	-1.466	1.955
14	Z	-0.227	0.925
24	X	-1.414	0.803
24	Y	-0.297	1.990
24	Z	0.943	0.943

Table 6.2: Orientations of Simulated Cluster.

Cluster	Width(kpc)	kpc per pixel	arc-seconds per pixel
5	3100	6.05	1.86
7	3124.62	6.1	1.87
9	2627.24	5.13	1.58
10	2333.14	4.56	1.4
11	2486.62	4.86	1.49
14	2519.62	4.92	1.51
24	2068.02	4.04	1.24

Table 6.3: Resolution data for cluster convergences.

## 6.2 Results for Calculated Shear

Table 6.4 lists the average shear values for each cluster projected perpendicular to the listed line of sight(LOS). Averaging is done in two regions, inside and outside of half of the virial radius. In both regions, the overall average shear of each projection has been calculated. These values are listed in the “Average” columns of Table 6.4. Next the absolute difference between the overall average of all twenty-one shear maps and the average for each individual shear map (“Average” column) is listed as the “Difference from Mean”. This difference from the overall mean value is also provided as a percentage of the mean to quantify the dispersion in shear values (“Percent Difference” column). In addition to this percent difference measure of variation, the standard deviation is listed below the average on the bottom of each column in Table 6.4.

For illustrative purposes, the effect of lensing by one of the clusters on a circular background source is calculated and illustrated as a shear map for the respective cases. At each point, the transformation matrix,  $A$ , is calculated using the corresponding convergence and shear values. From this matrix, the lengths of the lensed image axes are calculated using the eigenvalues of the transformation matrix, according to Equation (2.25). A circular background source is lensed to an ellipse with principal axes lying along the eigenvectors of the transformation matrix. Figures 6.1 - 6.4 provide two illustrations of the simulated lensing. Figures 6.2 & 6.4 show convergence maps for two different projections of cluster 5. Figures 6.1 & 6.3 show shear for these convergence maps. The lines in these plots show the semi-major axis of the lensed image of a circular source. The length of the lines represents the ratio of semi-minor to semi-major axes, where a unit length represents a circle. To provide visually useful images, the shear maps are produced by averaging semi-major axis position angles and axial ratios in eight-by-eight pixel bins, reducing the  $512^2$  grid to a  $64^2$  grid. To illustrate the average tangential alignment around mass points, the convergences for

		Shear					
Cluster	LOS	Average		Difference from Mean		Percent Difference	
		$< 0.5R_{vir}$	$> 0.5R_{vir}$	$< 0.5R_{vir}$	$> 0.5R_{vir}$	$< 0.5R_{vir}$	$> 0.5R_{vir}$
5	X	0.041	0.011	0.0052	0.0034	11	23
5	Y	0.044	0.012	0.0027	0.0027	5	18
5	Z	0.045	0.013	0.0015	0.0019	3	13
7	X	0.045	0.015	0.0013	0.0000	3	0
7	Y	0.049	0.016	0.0025	0.0014	5	9
7	Z	0.052	0.015	0.0051	0.0003	11	2
9	X	0.033	0.010	0.013	0.0045	29	30
9	Y	0.032	0.010	0.015	0.0047	32	32
9	Z	0.039	0.010	0.0081	0.0047	17	32
10	X	0.045	0.014	0.0019	0.0010	4	7
10	Y	0.056	0.015	0.0092	0.0001	20	1
10	Z	0.043	0.014	0.0036	0.0008	8	5
11	X	0.073	0.027	0.026	0.012	57	80
11	Y	0.087	0.028	0.041	0.013	88	88
11	Z	0.072	0.026	0.025	0.011	54	72
14	X	0.042	0.013	0.0050	0.0017	11	11
14	Y	0.042	0.013	0.0050	0.0015	11	10
14	Z	0.045	0.013	0.0017	0.0014	4	9
24	X	0.029	0.011	0.018	0.0036	38	24
24	Y	0.037	0.012	0.010	0.0029	21	20
24	Z	0.029	0.012	0.018	0.0032	38	22
Average		0.047	0.015	0.011	0.0036	22	24
Std. Dev.		0.015	0.0053	0.010	0.0038	22	25

Table 6.4: Average shear values for simulated clusters.

these two shear maps are shown as well, using a logarithmic scale. As each cluster was created in a region bound by the virial radius, the coordinates of the shear plots are given in terms of the virial radius, which may be found in Table 6.1. The average of this axial ratios is provided in Table 6.5.

Table 6.6 clearly demonstrates that there is a variation in shear caused simply by the fact that the clusters are non-spherical. In Table 6.6, the difference in the average shear between two quadrants of the clusters was found in the region outside of  $0.5R_{vir}$ . In the spherical case, the difference should be zero. Therefore, the shear

was calculated for a spherical NFW cluster with the same virial mass, radius and concentration using the formulae given by Wright & Brainerd 2000. The difference between the shear values is then presented as a percentage of this spherical result in Table 6.6.

		Image Axial Ratios					
Cluster	LOS	Average		Difference from Mean		Percent Difference	
		$< 0.5R_{vir}$	$> 0.5R_{vir}$	$< 0.5R_{vir}$	$> 0.5R_{vir}$	$< 0.5R_{vir}$	$> 0.5R_{vir}$
5	X	0.92	1.0	0.011	0.026	1	3
5	Y	0.91	0.98	0.0055	0.0043	0.6	0.4
5	Z	0.91	0.97	0.0033	0.0027	0.4	0.2
7	X	0.91	0.97	0.0023	0.0010	0.3	0.1
7	Y	0.90	0.97	0.0060	0.0038	0.7	0.4
7	Z	0.90	0.97	0.011	0.0016	1	0.1
9	X	0.93	0.98	0.026	0.0079	3	0.8
9	Y	0.94	0.98	0.030	0.0082	3	0.8
9	Z	0.92	0.98	0.017	0.0082	2	0.8
10	X	0.91	0.97	0.0043	0.00090	0.5	0.09
10	Y	0.89	0.97	0.017	0.0011	2.8847	0.1
10	Z	0.91	0.97	0.0062	0.00050	0.7	0.05
11	X	0.86	0.95	0.052	0.024	6	2
11	Y	0.83	0.95	0.080	0.026	9	3
11	Z	0.85	0.95	0.053	0.022	6	2
14	X	0.92	0.97	0.0098	0.0023	1	0.2
14	Y	0.92	0.97	0.0098	0.0018	1	0.2
14	Z	0.91	0.97	0.0037	0.0017	0.4	0.2
24	X	0.94	0.98	0.036	0.0060	4	0.6
24	Y	0.93	0.98	0.019	0.0047	2	0.5
24	Z	0.94	0.98	0.035	0.0052	4	0.5
Average		0.9	1	0.02	0.008	2	0.8
Std. Dev.		0.03	0.01	0.02	0.009	2	0.9

Table 6.5: Average image axial ratio values for simulated clusters.

Cluster	LOS	Percent Difference
10	X	0
14	Z	1
24	Z	3
10	Y	3
24	Y	4
5	X	4
7	X	4
11	X	5
9	X	7
7	Z	8
14	X	9
5	Z	9
7	Y	9
9	Y	10
9	Z	10
11	Y	11
14	Y	13
10	Z	16
5	Y	18
24	X	27
11	Z	44
Average		10

Table 6.6: Difference in shear between quadrants as a percentage of the spherical cluster value

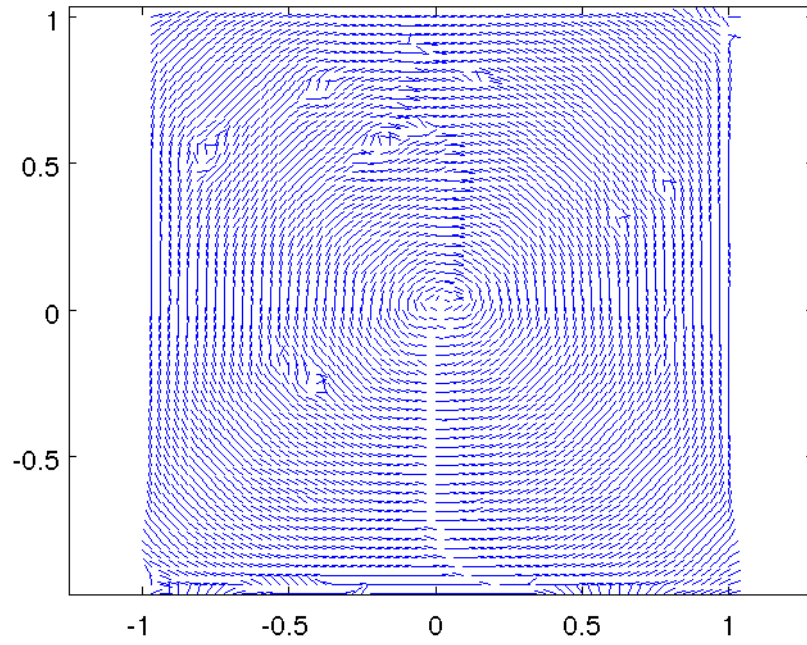


Figure 6.1: Shear map of cluster 5 projected perpendicular to the X-axis. Axes are labeled in units of the virial radius.

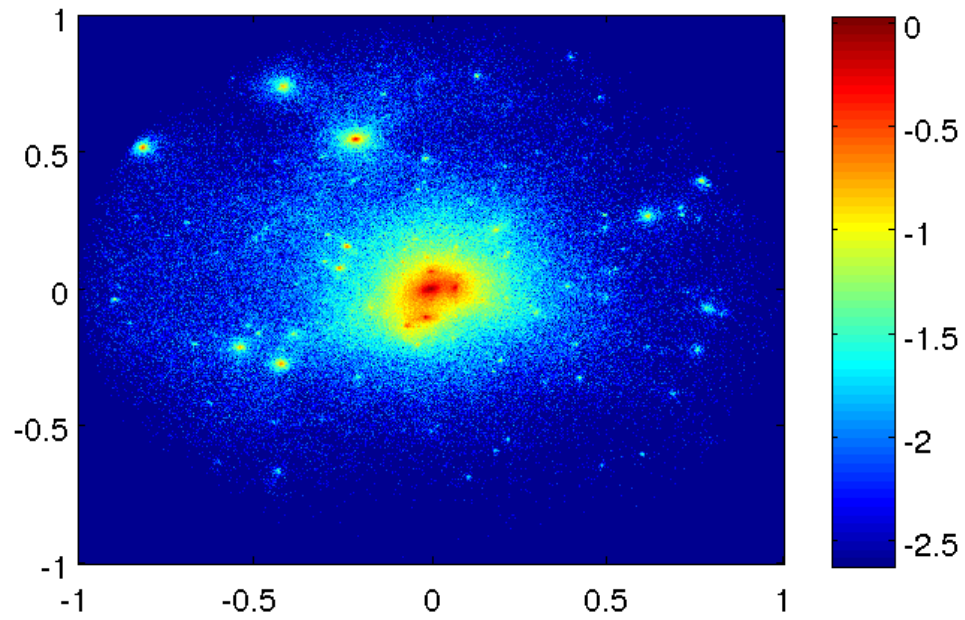


Figure 6.2: Convergence of cluster 5 projected perpendicular to the X-axis. Axes are labeled in units of the virial radius.

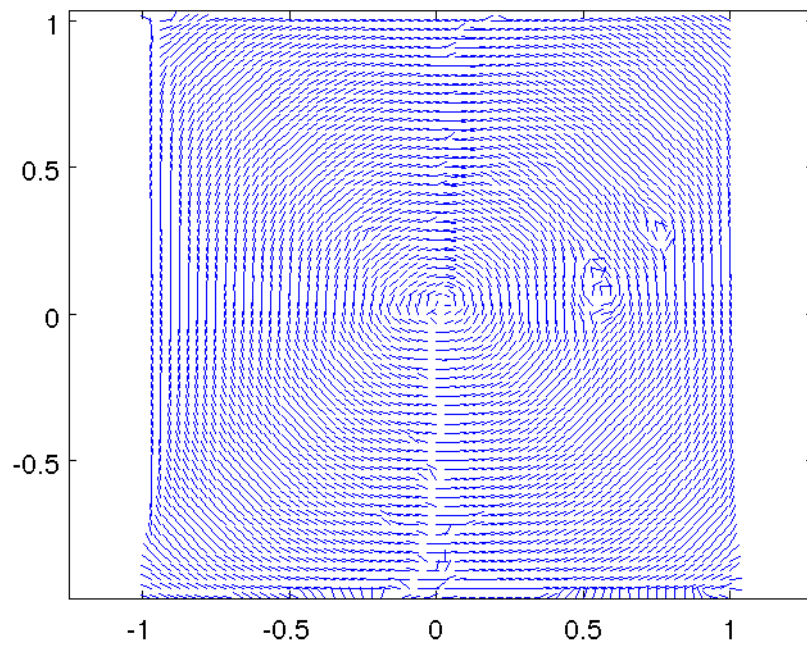


Figure 6.3: Shear map of cluster 5 projected along the Z-axis. Axes are labeled in units of the virial radius.

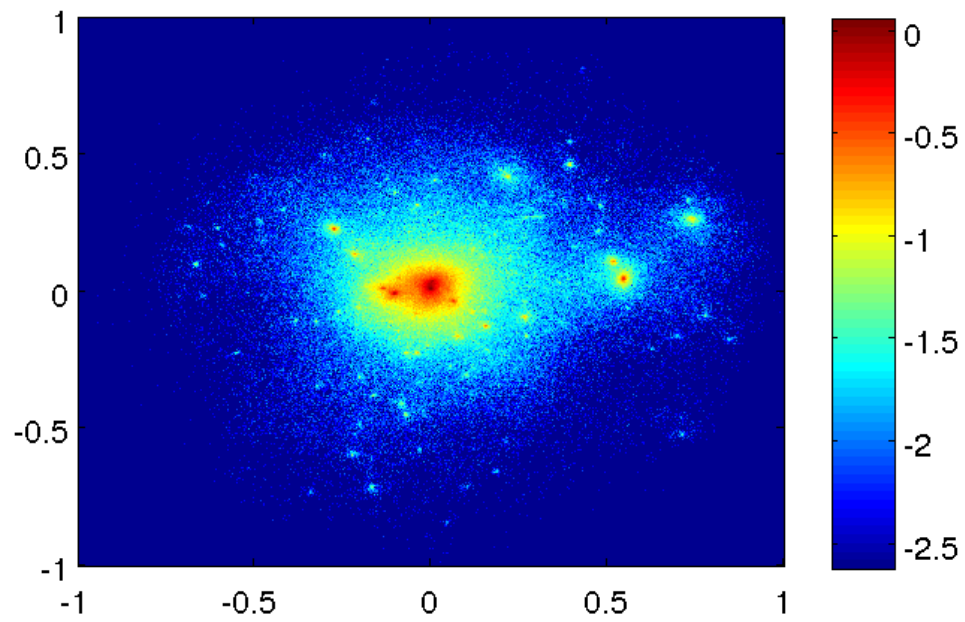


Figure 6.4: Convergence of cluster 5 projected perpendicular to the Z-axis. Axes are labeled in units of the virial radius.

## 7 Discussion

Using the shear data produced by the simulated clusters, one may deduce traits which could be observed. Shear itself exhibits dispersion beyond the levels of error indicated by the analytical NFW simulation, displayed in Figure 5.3. For the analytical NFW, the average percent difference of shear within half of the virial radius is 4%. However, the average percent difference for the clusters is 22%. Outside of half of the virial radius<sup>17</sup>, this average percent difference rises slightly to 24%. While one would first suspect that this variation is due to the differences in mass included in this set of clusters, Figure 7.1 shows the mass alone cannot account for the dispersion in shear. Additionally, Figure 7.2 shows no correlation between shear and concentration. Indeed, the axial ratio,  $s$ , seems to have the greatest impact on dispersion of shear. Average shear varies directly with  $s$  with two out-lying cases. Cluster 11 has exceedingly high shear values compared to the remaining of clusters. However, this cluster has the largest concentration, being nine percent higher than the mean, and has a total mass near the average of the set of clusters. While cluster 10 has a relatively high  $s$  value, it also has the second lowest mass, at 33% less than the mean, and shares the lowest concentration, along with cluster 9.

Observational mass reconstruction methods rely on measurements of image ellipticity and orientation. Shear maps presented in Section 6.2 distinctly show tangential alignment of images, characteristic of weak lensing. Lumps in the clusters are revealed in the shear maps through these alignments. The shear data was calculated with resolutions averaging 1.56 arc-seconds. As this resolution angle is much larger than is currently available, for example with the Hubble Ultra Deep Field (Beckwith et al. 2006), such sub-structures should be resolvable.

While tangential alignment distinctly outlines mass peaks, the overall effect of

---

<sup>17</sup>In the remainder of the text, statistical analysis will focus on the region outside of half of the virial radius, as this is more pertinent to weak lensing.

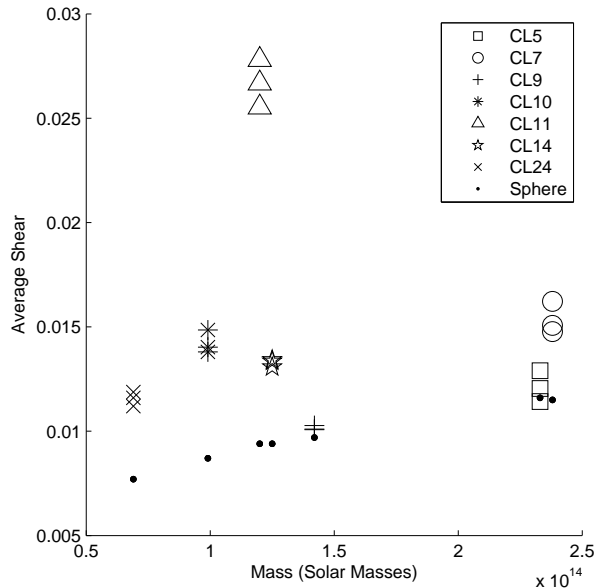


Figure 7.1: Plot of corresponding shear and mass values. Masses are given in units of  $10^{14} h^{-1} M_{\odot}$

mass isodensity ellipticity dispersion on the entire system as a whole seems likely to provide the greatest observational challenge. In the outer region,  $r > R_{vir}$ , Figure 7.5 shows a less distinct dependence of convergence on  $s$  than that of shear. Figures 7.6 and 7.7 show the correlation between the convergence and total mass and concentration, respectively. In the regions shown here, where the distance is greater than half of the virial radius, the concentration dominates the convergence trend. Ellipticity, measured by  $s$ , shows some connection to the variation of the convergence, though less direct than the concentration.

Combining the density parameter effects on convergence and shear shows the difficulty in accurately reconstructing convergence from shear values. Figure 7.8 demonstrates that a range of shear values can produce the same convergence values, with variations due to differences in ellipticity and concentration. From an observational standpoint, as described in Section 3.4, this convergence ambiguity is reflected in the

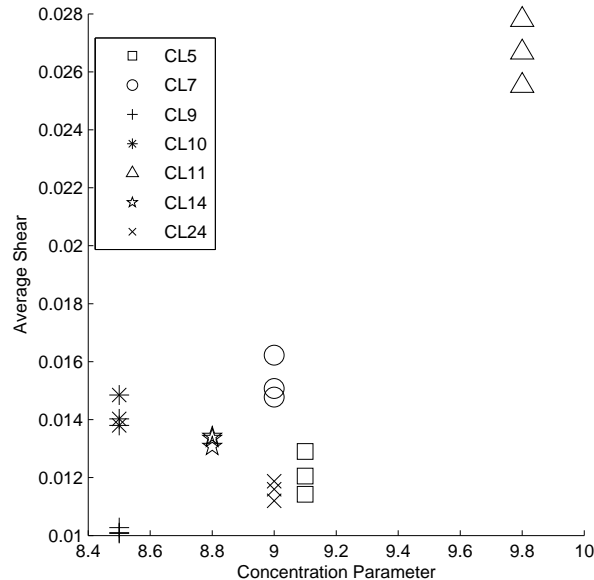


Figure 7.2: Plot of corresponding shear and concentration values.

concentration of image ellipticity values, with an average percent difference of just under 1%, compared to 24% for shear.

As mass reconstruction methods rely on averaging image ellipticity values, the results presented here demonstrate the difficulty in distinguishing mass density ellipticity from noise and error. Supplementing the previously demonstrated mass density dispersion (cf Allgood et al. 2006), shear has been shown to exhibit dispersion about the mean, which correlates strongly with the isodensity axial ratio,  $s$ , in a manner similar to cluster mass. On the other hand, in regions where weak lensing is best applied, distances greater than  $0.5R_{vir}$ , there is little corresponding dispersion in image ellipticity, which is used to reconstruct convergence values. In this image ellipticity concentration lies the observational challenge. For the clusters examined here, circular sources underwent an ellipticity change to an image axial ratio of 0.97, on average. Additionally, the variation within the set of twenty-one convergences was only 1%.

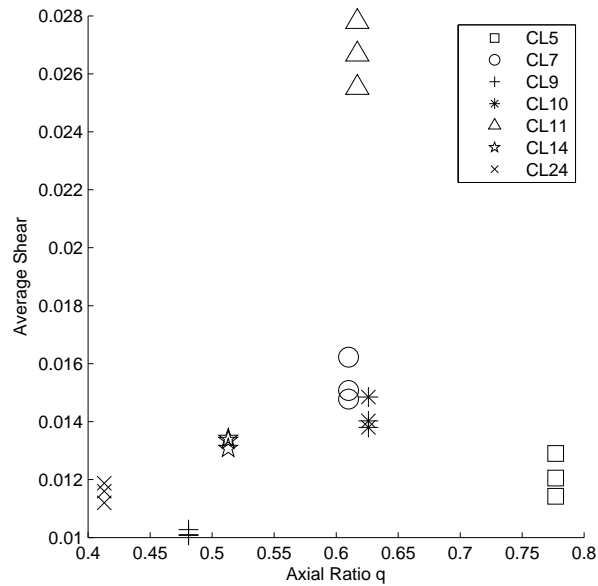


Figure 7.3: Plot of corresponding shear and axial ratio  $q$  values.

Therefore, to make these distinctions, one would have to resolve ellipticity changes in images on the order of roughly half of a percent, when the image axial ratios vary from being circular by less than 0.03. As presented here, mass reconstruction must be performed with the understanding that there is a notable variance in convergence values, alongside the reliable mass peak location resolution.

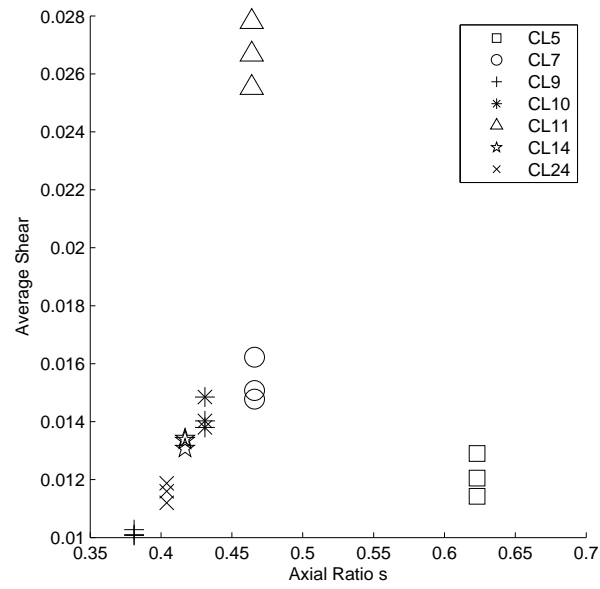


Figure 7.4: Plot of corresponding shear and axial ratio  $s$  values.

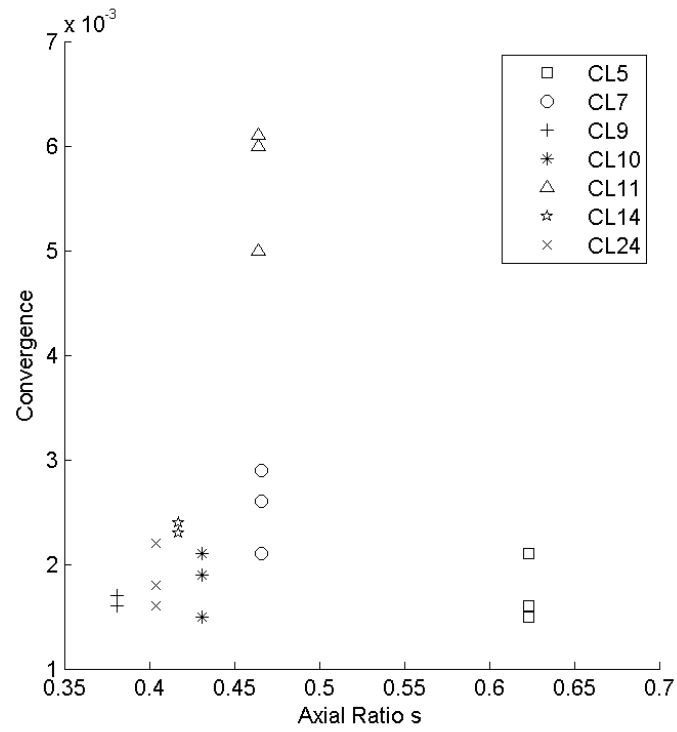


Figure 7.5: Plot of corresponding convergence and axial ratio  $s$  values.

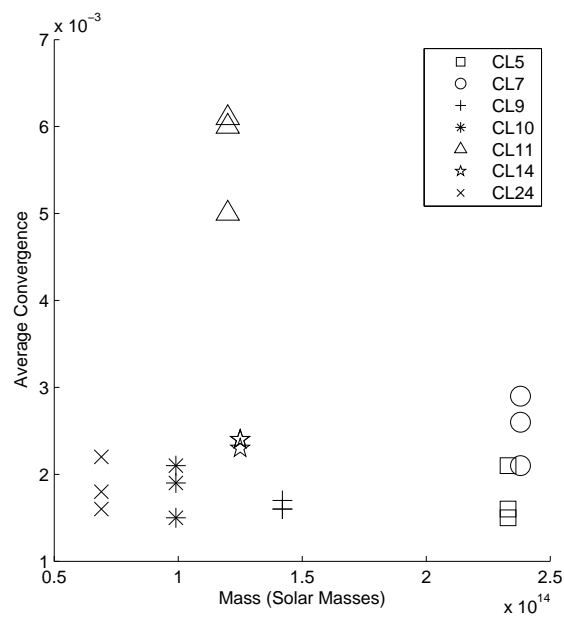


Figure 7.6: Plot of corresponding convergence and total mass values. Mass is given in units of  $10^{14} h^{-1} M_{\odot}$

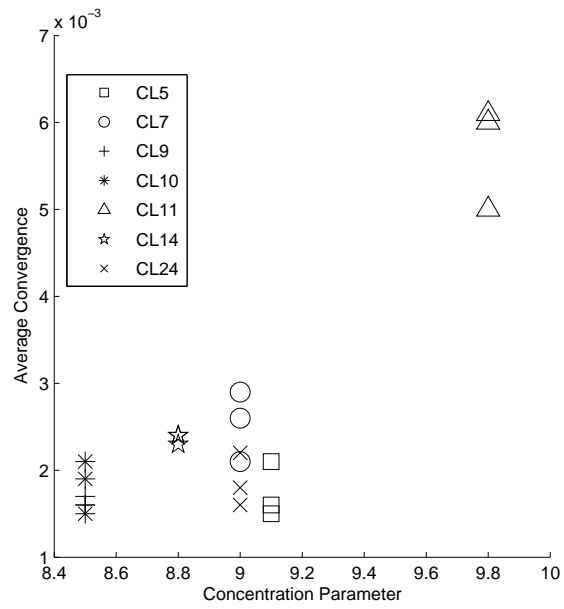


Figure 7.7: Plot of corresponding convergence and concentration parameter values.

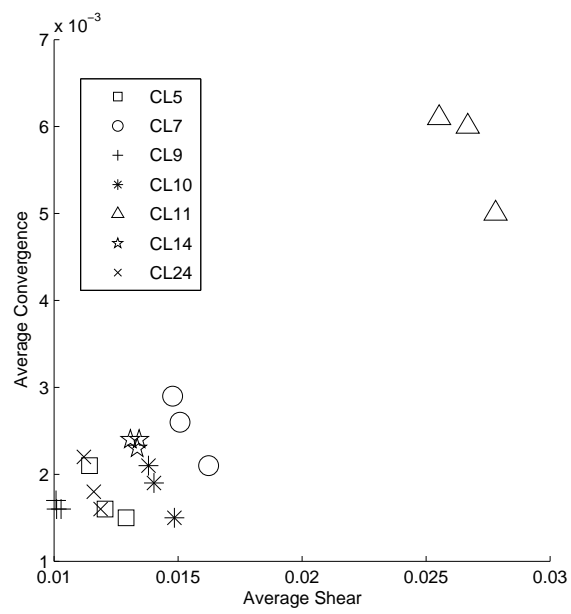


Figure 7.8: Plot of corresponding convergence and shear parameter values, for distances greater than  $0.5R_{vir}$ .

## 8 Summary

Variation in the shape of dark matter halo structures, as well as the presence of substructure, has been demonstrated for galaxy clusters. Meanwhile, average values of shear are used to reconstruct mass profiles based on observed cluster images. Therefore, an understanding of how shape variation and substructure of the dark matter halos of galaxy clusters effect average shear can help improve mass reconstruction. In order to characterize this effect, gravitational lensing was simulated for seven different simulated dark matter halos, including six clusters and one group. Virial masses ranged from  $6.9 * 10^{13} h^{-1} M_{\odot}$  to  $2.38 * 10^{14} h^{-1} M_{\odot}$  with an average of  $1.5 * 10^{13} h^{-1} M_{\odot}$ . Concentration ranged from 8.5 to 9.8, with an average of 9.0. For each of the clusters, isodensity regions are notably triaxial ellipsoids. Within this set of clusters, the ratio of the principle axes varies, as shown in Table 6.1.

Two simulation methods were used to study the gravitational lensing of galaxy clusters. Both methods simulate lensing for projected mass distributions, or convergence maps. One method uses the integration of deflection angles for the entire mass distribution. Using ray-tracing, graphical representations of lensing may be produced. A BOINC project was created to improve the computation speeds of this simulation method. All of the ray-trace diagrams in this study were produced using this simulation method. The second method produces a shear map for each convergence map through the partial differential equations given in Section 5.

Variance in shear is demonstrated for the set of seven clusters. The average shear for each cluster was found for the region outside of half of the virial radius. For the set of twenty-one convergence maps, shear varied about a mean of 0.015 with a standard deviation of 0.0053. Shear values vary by as much as 24% from the mean. By comparing adjacent quadrants, shear variation is shown to be the result of the ellipsoidal nature of the dark matter halo. If the halo was in fact spherically symmetric, the difference between two adjacent quadrants of the shear map should

be zero. However, as shown in Table 6.6, this is not the case for these clusters. When presented as a percentage of the shear value of the corresponding spherical case, the difference varies among the clusters with an average of 10%. For each of the parameters of the matter distribution, listed in Table 6.1, there is little correlation with the average shear, with the exception of the axial ratio  $s$ , which shows an almost linear relationship (cf Figure 7.4). As demonstrated here, especially illustrated in Figure 7.8, a range of convergences can produce the same average shear value simply by varying the shape of the halo. Therefore, mass reconstructions must include studies of shape in order to more accurately find galaxy cluster mass.

Since this work suggests that attention must be paid to the shape of dark matter halos when reconstructing mass profiles via gravitational lensing, a study could now be done to use simulated lensing of realistic background images. From such images, one could then carry out mass reconstruction through commonly used methods to directly observe the effect the shear variations noted on the reconstruction of mass profiles. Additionally, analyzing more clusters would help further constrain statistics. Also, applying this study to single galaxies could extend the understanding of the effects of shape to galaxy-galaxy lensing techniques, as galaxy dark matter halos demonstrate a broad dispersion in shape like galaxy clusters.

## A Generation of Mass Distributions for Numerical Simulation

One method of producing mass distributions is through the quasi-random placement of particles according to a probability function based on the mass density. Press et al. 1992 outline methods of generating random number, including uniform deviates and random number based on a probability function. For a mass density,  $\rho(r, \phi, \theta)$ , a distribution of particles can be created through the use of a random number generator, limited in accuracy by the number of particles placed in the distribution. The density function,  $\rho(r, \phi, \theta)$ , is treated as a probability function, which is normalized to provide the desired total mass. Using equally probable random numbers, from a set hereafter denoted by  $\mathbb{U}$ , particle positions may be found using a probability function derived from the density. Namely, if for  $\rho = \rho(r)$ , a function,  $Q(r)$ , can be found, such that  $x = Q(r)\epsilon \mathbb{U}$ , then  $\rho(x) = Q^{-1}(x)$ . This method relies on the existence of  $Q(r)$ . Additionally, for spherically symmetric cases, distances are selected from this probability distribution, while azimuthal and polar coordinates are selected from  $\mathbb{U}$ . However, in distributions lacking this symmetry, for example elliptical coordinates, random numbers must be transformed into those coordinates, e.g.  $R = \sqrt{x^2 + \frac{y^2}{q^2} + \frac{z^2}{s^2}}$  (cf Section 3.3.2). For the NFW distribution,

$$\rho(r' \equiv \frac{r}{r_s}) \propto \frac{1}{r'(1+r')^2}. \quad (\text{A.1})$$

For this function, there exists a transformation function,

$$Q(r') = \frac{1}{1+r'} + \ln(r') - \ln(1+r'). \quad (\text{A.2})$$

The Singular isothermal sphere requires only straight forward integration of  $\frac{1}{r^2}$ , but, like the NFW profile, normalization must be used to provide to desired total mass.

Additionally, the uniform ellipse, used in Section 4.5, can be produced by selecting a random position from  $\mathbb{U}$  and retaining points only if they are located within the ellipse.

## B Calculation of Lensing Properties of the NFW Profile

The NFW profile has been shown to accurately characterize dark matter halos. Therefore, to compare the simulation data calculated here, it is necessary to obtain the corresponding results from the NFW model. While analytical results for shear, convergence and total mass are available for spherically symmetric NFW distributions (Wright & Brainerd 2000), ellipsoidal distributions are complicated enough to require calculation by numerical integration instead.

While studying the kinematics of elliptical galaxies, Binney 1985 showed that for triaxial ellipsoids, the surface density may be simplified to a one-dimensional function. Let

$$a^2 \equiv x^2 + \frac{y^2}{q_{2D}^2} \quad (\text{B.1})$$

$$q_{2D} \equiv \sqrt{\frac{A + C - \sqrt{(A - C)^2 + B^2}}{A + C + \sqrt{(A - C)^2 + B^2}}} \quad (\text{B.2})$$

$$A \equiv \frac{\cos^2 \theta}{s^2} \left( \sin^2 \phi + \frac{\cos^2 \phi}{q^2} \right) + \frac{\sin^2 \theta}{q^2} \quad (\text{B.3})$$

$$B \equiv \cos \theta \sin 2\phi \left( 1 - \frac{1}{q^2} \right) \frac{1}{s^2} \quad (\text{B.4})$$

$$C \equiv \left( \frac{\sin^2 \phi}{q^2} + \cos^2 \phi \right) \frac{1}{s^2}. \quad (\text{B.5})$$

Then the mass density can be found according to

$$\Sigma(a) = \frac{2}{\sqrt{f}} \int_0^\infty \rho(z''^2 + a^2) dz'', \quad (\text{B.6})$$

where

$$f \equiv \sin^2 \theta \left( \cos^2 \phi + \frac{\sin^2 \phi}{q^2} \right) + \frac{\cos^2 \theta}{s^2} \quad (\text{B.7})$$

and  $\rho$  is the NFW mass density according to Equation (3.11), using ellipsoidal coordinates. Integration gives (Flores, private communication)

$$\Sigma(a) = \frac{2\rho_s R_s}{\sqrt{f}} \begin{cases} \frac{\operatorname{arctanh}(\sqrt{1-a^2}) - \sqrt{1-a^2}}{(1-a^2)^{\frac{3}{2}}} & , a < 1 \\ \frac{\sqrt{a^2-1} - \operatorname{arctan}(\sqrt{a^2-1})}{(a^2-1)^{\frac{3}{2}}} & , a > 1 \end{cases} , \quad (\text{B.8})$$

where  $a$  is written in terms of  $R_s$ .

As a means of studying light deflection angles for homoeoidal mass distributions, particularly to simplify numerical calculation, Schramm 1990 extends the projection methods of Binney 1985 through the use of potential theory. Schramm 1990 takes advantage of simplifications in the potential that arise for confocal homoeoidal mass densities. For an ellipse of the form,

$$\frac{x^2}{a^2} + \frac{y^2}{b^2} = 1 \quad (\text{B.9})$$

a confocal ellipse is one such that

$$\frac{x^2}{a^2 + \lambda} + \frac{y^2}{b^2 + \lambda} = 1 \quad , \quad \lambda > 0 \quad , \quad (\text{B.10})$$

while homoeoidal ellipses are given by

$$\frac{x^2}{(ma)^2} + \frac{y^2}{(mb)^2} = 1 \quad , \quad m \geq 1 \quad . \quad (\text{B.11})$$

For such homoeoidal ellipsoids, Schramm 1990 finds the deflection angle to be

$$\hat{\alpha}_x = -\frac{8\pi G a b}{c^2} \int_0^{m_0} \frac{p'^2}{a' b'} \frac{x}{a'^2} \Sigma(m) m dm \quad (\text{B.12})$$

$$\hat{\alpha}_y = -\frac{8\pi G a b}{c^2} \int_0^{m_0} \frac{p'^2}{a' b'} \frac{y}{b'^2} \Sigma(m) m dm , \quad (\text{B.13})$$

where

$$a'^2 \equiv a^2 + \lambda \quad (\text{B.14})$$

$$b'^2 \equiv b^2 + \lambda \quad (\text{B.15})$$

$$p'^2 \equiv \frac{a^4 b^4}{x^2 b^4 + y^2 a^4} \quad (\text{B.16})$$

$$m_0 \equiv \sqrt{x^2 + \frac{y^2}{q_{2D}^2}}. \quad (\text{B.17})$$

This result allows one to calculate the deflection angle at any point for a homoeoidal distribution, such as the NFW profile, through numerical integration. Additionally, this approach can be extended to the calculation of shear through differentiation of the deflection angle, using Equations (4.2) and (4.3).

## References

- Allgood, B., Flores, R., Primack, J., Kravtsov, A., Wechsler, R., Faltenbacher, A., & Bullock, J. 2006, MNRAS, 367, 1781
- Anderson, D. 2004, in 5th IEEE/ACM International Workshop on Grid Computing, Pittsburgh
- Aubert, D., Amara, A., & Metcalf, R. 2007, MNRAS, 376, 113
- Bartelmann, M. 1996, A&A, 313, 697
- Beckwith, S. V. W., Stiavelli, M., Koekemoer, A. M., Caldwell, J. A. R., Ferguson, H. C., Hook, R., Lucas, R. A., Bergeron, L. E., Corbin, M., Jogee, S., Panagia, N., Robberto, M., Royle, P., Somerville, R. S., , & Sosey, M. 2006, ApJ, 132, 1729
- Bekenstein, J. D. 2004, Phys. Rev. D, 70, 083509
- Binney, J. 1985, MNRAS, 212, 767
- Brownstein, J. & Moffat, J. 2006, MNRAS, 367, 527
- Clowe, D., Bradac, M., Gonzalez, A., Markevitch, M., Randall, S., Jones, C., & Zaritsky, D. 2006, ApJ, 648, L109
- Clowe, D., Gonzalez, A., , & Markevitch, M. 2004, ApJ, 604, 596
- Demianski, M., de Ritis, R., Marino, A., & Piedipalumbo, E. 2003, 411, 33
- Dubinski, J. & Carlberg, R. 1991, ApJ, 378, 496
- Dyson, F. W., Eddington, A. S., & Davidson, C. 1920, RSPTA, 220, 291
- Einstein, A. 1911, Ann. Phys., 35
- . 1916, Ann. Phys., 49

- Flores, R., Allgood, B., Kravtsov, A., Primack, J., Buote, D., & Bullock, J. 2007, MNRAS, 377, 883
- Gavazzi, R., Treu, R., Rhodes, J., Koopmans, L., Bolton, A., Burles, S., Massey, R., & Moustakas, L. 2007, ApJ, 667, 176
- Hammer, F. 1991, ApJ, 383, 66
- Hinshaw, G., Weiland, J. L., Hill, R. S., Odegard, N., Larson, D., Bennett, C. L., Dunkley, J., Gold, B., Greason, M. R., Jarosik, N., Komatsu, E., Nolta, M. R., Page, L., Spergel, D. N., Wollack, E., Halpern, M., Kogut, A., Limon, M., Meyer, S. S., Tucker, G. S., , & Wright, E. L. 2009, ApJS, 180, 225
- Hoekstra, H., Yee, H., & Gladders, M. 2004, ApJ, 606, 67
- Jain, B., Seljak, U., & White, S. 2000, ApJ, 530, 547
- Jarosik, N., Bennett, C. L., Dunkley, J., Gold, B., Greason, M. R., Halpern, M., Hill, R. S., Hinshaw, G., Kogut, A., Komatsu, E., Larson, D., Limon, M., Meyer, S. S., Nolta, M. R., Odegard, N., Page, L., Smith, K. M., Spergel, D. N., Tucker, G. S., Weiland, J. L., Wollack, E., & Wright, E. L. 2010, ApJS Submitted (preprint arXiv:1001.4744)
- Kaiser, N. 1995, ApJ, 439, L1
- Kaiser, N. & Squires, G. 1993, ApJ, 404, 441
- Kent, S. 1987, ApJ, 93, 816
- Lasky, P. D. & Fluke, C. J. 2009, MNRAS, 296, 2257
- LSST. 2010, Science Book, last retrieved from <http://www.lsst.org> on 03/16/2010
- Lynden-Bell, D. 1967, MNRAS, 136, 101

- Lynds, R. & Petrosian, V. 1986, *Bull. AAS*, 18, 1014
- . 1989, *ApJ*, 336, 1
- Mandelbaum, R., Hirata, C., Broderick, T., Seljak, U., & Brinkmann, J. 2006, *MNRAS*, 370, 1008
- Milgrom, M. 1983, *ApJ*, 270, 365
- Miller, J. S. & Goodrich, R. W. 1988, *Nature*, 331, 685
- Myles, A. 1999, *Nature*, 401
- Natarajan, P. & Refregier, A. 2000, 538
- Navarro, J., Frenk, C., & White, S. 1996, *ApJ*, 462, 563
- Pointecouteau, E. & Silk, J. 2005, *MNRAS*, 364, 654
- Press, W., Teukolsky, S., & Vetterling, W. 1992, *Numerical Recipes in C*, Vol. 2 (Cambridge)
- Qian, B., Raman, S., Das, R., Bradley, P., McCoy, A., Read, R., & Baker, D. 2007, *Nature*, 450, 259
- Refsdal, S. 1964, *MNRAS*, 128, 307
- Rubin, V. & Ford, W. 1970, *ApJ*, 159, 379
- Rusin, D., Kochanek, C., & Keeton, C. 2003, *ApJ*, 595, 29
- Schneider, P. & Bartelmann, M. 1997, *MNRAS*, 286, 696
- Schneider, P., Ehlers, J., & Falco, E. E. 1999, *Gravitational Lenses* (Springer)
- Schneider, P., Kochanek, C., & Wambsganss, J. 2006, *Gravitational Lensing: Strong, Weak and Micro* (Springer)

Schramm, T. 1990, *A&A*, 231, 19

Shu, F. H. 1977, *A&A*, 214, 488

Soldner, J. 1804, *Berliner Astron. Jahrb.*, 0, 161

Treu, T. & Koopmans, L. 2002, *ApJ*, 575, 87

Tyson, J. A., Wenk, R. A., & Valdes, F. 1990, *ApJ*, 349, L1

Wright, C. & Brainerd, T. 2000, *ApJ*, 534, 34

Zwicky, F. 1937a, *Phys. Rev.*, 51, 290

—. 1937b, *ApJ*, 86, 217

## Vita

David Raymond Coss was born in Monroe, Michigan on June 29, 1982. In December 2004, he received a B.A. degree in Physics and German from Belmont University in Nashville, Tennessee. He completed a M.S. degree in Physics in May 2007 at the University of Missouri - St. Louis. In May 2010, he received Ph.D. degree from the University of Missouri - St. Louis and Missouri University of Science and Technology.